High-speed atomic force microscopy

doi: 10.1143/JJAP.51.08KA02

High-speed Atomic Force Microscopy

Toshio Ando[1,2], Takayuki Uchihashi[1,2], Noriyuki Kodera[2]

[1]Department of Physics, Kanazawa University, Kakuma-machi, Kanazawa 920-1192, Japan

[2]Bio-AFM Frontier Research Center, Kanazawa University, Kakuma-machi, Kanazawa 920-1192, Japan

High-speed atomic force microscopy (HS-AFM) now comes of age. It allows us to directly visualize the structure and dynamics of biological molecules in physiological solutions, at subsecond to sub-100 ms temporal resolution. In fact, dynamically acting molecules such as myosin V walking on an actin filament and bacteriorhodopsin in response to light are successfully visualized. High-resolution molecular movies reveal dynamic behavior of molecules in action in great detail. Inferences no longer have to be made from static snapshots of molecular structures and dynamic behavior of optical markers attached to biomolecules. In this review, we first describe theoretical considerations for the highest possible imaging rate, then summarize techniques involved in HS-AFM and highlight recent imaging studies. Finally, future challenges to explore are briefly discussed.

Keywords: high-speed AFM, AFM, bioimaging, proteins, dynamic imaging

1. Introduction

The function of proteins is tightly related to their structures, and thus, structural biologists have been determining the detailed structure of proteins. However, the obtained structures are essentially static, whereas proteins are dynamic in nature. Dynamic behavior of proteins in action has been mainly studied by single-molecule fluorescence microscopy.[1,2] A fluorescent spot emitted from a fluorophore attached to a specific locus of a protein is recorded on video and the time sequence of its position (or polarization angle) is analyzed in high precision. Nevertheless, protein molecule themselves are invisible in the observations. Hence, the simultaneous observation of structure and dynamics has long been infeasible. We have to infer how proteins operate to function from gleaned data with significant resolution gaps. The inference is often affected by assumptions and interpretations of the date, and therefore, different conclusions are sometimes derived from the same experimental data. We often need many years until reaching a convincing conclusion on the functional mechanism of a protein. Thus, it is evident that we should develop more direct methods that can provide great details of molecular action without intricate analyses and interpretations.

Atomic force microscopy (AFM) is unique in its capability of directly capturing high resolution images of vital biological samples in aqueous solutions.[3,4] AFM was thus expected to play a role in bridging the gap between structural biology and single-molecule biophysics. However, AFM was not able to meet this expectation because of its low imaging rate. Visualization of a sample by AFM requires acquisition of sample height information over many points on the sample surface (see Fig. 1). During the acquisition at each point, the following operations are carried out. A stylus probe attached to the free end of a cantilever is brought into contact with the sample.

Mechanical response of the cantilever upon this contact (change in, e.g., deflection, oscillation amplitude, oscillation phase, or resonant frequency, depending on the operation mode of AFM used) is measured and then the sample stage is finally moved in the z-direction to recover the mechanical state of the cantilever back to a given condition (*i.e.*, set point) through feedback control. For this recovery, the closed feedback loop spends a certain amount of time mainly because of slow response of the mechanical devices (*i.e.*, cantilever and z-scanner). This series of operations is repeated many times for different sample surface points during lateral scanning of the sample stage. Thus, it takes a long time (at least 30 s) to capture an image of the sample. Molecules moving on the substrate surface are, therefore, blurredly imaged or cannot be imaged at all.

Hansma's group and our group independently commenced around 1993 to develop high-speed AFM (HS-AFM) in the tapping mode. Various devices and techniques, such as small cantilevers,[5-10] high-speed scanners[8,9,11-16], active damping[16,17] and feedback control[16,18] techniques, and electronics[8,9,12,13,16-21] have been developed. After a proof-of-principle stage, HS-AFM now comes of age.[22-24] Although the speed performance depends on imaging conditions, it can generally capture an image of a protein molecule within 100 ms or less. Importantly, the structure and function of fragile proteins are not disturbed by the interaction with an oscillating cantilever tip.[22-24] This high-speed and low-invasive performance provides a new opportunity to visualize dynamically functioning protein molecules in great details. As has been demonstrated in recent imaging studies,[22-33] the visualized dynamic images of proteins can provide information inaccessible with other approaches, giving a great insight into how the proteins function. Remarkably, the dynamic images can be interpreted

straightforward without intricate analyses and interpretations, making it possible to attain irrefutable conclusions. There seems no doubt that continued exploration of countless biological phenomena will be carried out using HS-AFM in the near future. The Review is written with intention of providing potential users of HS-AFM with the overview of techniques implemented in the instrument and with precautions and devices for successful imaging. The review also briefly discusses future challenges to overcome limitations of the current HS-AFM.

2. Highest Possible Imaging Rate

2.1 Feedback bandwidth

We chose the tapping mode among various operation modes of AFM such as contact, tapping, and frequency-modulation (FM) modes. In the tapping mode, the cantilever is oscillated in the z-direction at its first resonant frequency. The resulting intermittent contact between the tip and sample can eliminate friction force during lateral scanning and thus minimize damage and deformation of fragile biological samples. The FM mode, in which the cantilever is oscillated in the z-direction with small amplitude less than 1 nm, enables highly sensitive force detection. Nonetheless, the frequency detection is rather complicated and the detection speed is slower than the amplitude detection. In the tapping mode, the vertical tip force acting on the sample is controlled by a proportional-integral-derivative (PID) controller so that the cantilever oscillation amplitude (thus the tip-sample interaction force) is kept constant. Precise and fast feedback control is mandatory for fast and low-invasive imaging.

Fig. 2 shows devices contained in the closed feedback loop as well as time delays with each of which the corresponding device responds when used independently (*i.e.*,

time delay intrinsic to each device). The input to this feedback loop is variation of the sample height while the output is displacement of the z-scanner. The output from the PID controller is used as an image signal (*i.e.*, a sample height signal). The total sum of the intrinsic time delays is referred as the open-loop time delay (τ_{open}). The total delay in the closed feedback loop (τ_{close}) is different from τ_{open}. The relationship between them is approximately given as $\tau_{close} = 2\tau_{open}$, as far as the feedback gain is maintained at ~1.[16] The phase delay in the feedback loop θ_{close} is given by $\theta_{close} = 2\pi f\tau_{close}$, where f is the feedback frequency at which the z-scanner is displaced. The feedback bandwidth f_B is usually defined by the feedback frequency at which $\pi/4$ phase delay occurs in tracing the sample surface. Thus, we can derive the following relationship; $f_B = 1/(16\tau_{open})$. The main operation of the PID control is performed by the I-operation; *i.e.*, integration of error signals (difference between the cantilever oscillation amplitude A and its set point A_s). The P- and D-operations compensate the I-operation for its delay by a factor of $\alpha > 1$, so that the feedback bandwidth is modified as

$$f_B = \alpha/(16\tau_{open}). \qquad (1)$$

2.2 Excessive force

Under the condition of cantilever free oscillation amplitude A_0 and its set point A_s, a peak force F_p is exerted from the oscillating cantilever tip to the sample by $F_p = k_c(A_0^2 - A_s^2)^{1/2}/Q_c$, [25] where k_c is a spring constant and Q_c is a quality factor of the cantilever in water. This estimation is made under a provisional condition that no feedback delay occurs. How large excessive force is exerted onto the sample due to feedback delay? For simplicity, we assume that the sample has a sinusoidal surface corrugation characterized with wavelength λ in the x-direction and the maximum height h_0 (see Fig.

3). When the sample stage is moved at velocity V_s in the x-direction, the sample height h right under the cantilever tip changes as $h(t) = h_0/2 \times \sin(2\pi V_s t/\lambda)$. When the cantilever tip can always touch the sample surface at the bottom of swing, the z-scanner moves as $z(t) = -h_0/2 \times \sin(2\pi V_s t/\lambda - \theta_{close})$. The difference between $h(t)$ and $-z(t)$ is the feedback error ("residual topography", ΔS) and expressed as

$$\Delta S(t) = h(t) + z(t) = h_0 \sin\frac{\theta_{close}}{2} \cos\left(2\pi V_s t / \lambda - \frac{\theta_{close}}{2}\right). \qquad (2)$$

The cantilever tip feels this residual topography in addition to a constant height of $A_0(1 - r)$, where r is the dimensionless set point (*i.e.*, $r = A_s/A_0$). Therefore, when feedback delay occurs, the maximum excessive force is exerted by $\sim k_c h_0 \sin(\theta_{close}/2)/Q_c$ at an uphill region of the sample. On the other hand, when $\Delta S(t) + A_0(1 - r) < 0$ at a downhill region of the sample, the tip completely detaches from the sample surface and time elapses until the tip lands on the surface again (i.e., parachuting). During parachuting, the sample height information is completely lost. Therefore, the time over which parachuting continues also participates in the closed-loop time delay.

2.3 Highest possible imaging rate

The highest possible imaging rate (i.e, highest possible frame rate) R_{max} depends on the feedback bandwidth f_B as well as on the imaging condition, the spatial frequency of the sample surface corrugation ($1/\lambda$) to be imaged, and the sample fragility. The imaging condition is given by the scan range in the x-direction (W) and the number of scan lines (N). When the x-scanner is displaced at velocity V_s, the z-scanner is scanned at frequency $f = V_s/\lambda$ and one image is captured with time $T = 2NW/V_s$. Thus, we obtain $T = 2NW/\lambda f$. When the sample is strong enough so that it is not affected by the excessive tip force due to $\pi/4$ phase delay, the feedback frequency f can go up to f_B. In this case,

we obtain $R_{max} = \lambda f_B/(2NW)$. In reality, fragile biological molecules would not withstand a large excessive force. By denoting by θ_{max} the maximum phase delay allowable for a fragile molecule, the highest possible imaging rate is given by

$$R_{max} = 2\theta_{max}\lambda f_B/(\pi NW). \quad (3)$$

Here, we have to note that the mechanical quantity affecting the sample (i.e., altering the momentum) is not the force itself but the impulse of force, *i.e.*, force × the time period over which the force is applied. For our small cantilevers with resonant frequency 1.2 MHz in water, the force applying period is ~100 ns or less.

3. Time Delays

3.1 Time delay with cantilever

As seen below, the cantilever is the most influential delay component among devices in the feedback loop (Fig. 2). First of all, the tip, which is oscillating at the first resonant frequency of the cantilever f_c, should tap the sample surface at least once per pixel, and thus we obtain $f_c > 2N_{p\text{-}x}N_{p\text{-}y}/T$, where $N_{p\text{-}x}$ and $N_{p\text{-}y}$ are the numbers of pixels in the x- and y-directions, respectively. For example, to capture an image with 100 × 100 pixels at 25 fps, f_c should be at least 500 kHz in an aqueous solution, when this tapping issue is only considered. Upon tapping, a brief step-wise force is exerted to the cantilever. The cantilever responds to this force with a response time given by $\tau_c = Q_c/(\pi f_c)$. In addition, it takes time to measure the cantilever oscillation amplitude and its minimum time τ_m is given by $\tau_m = 1/(2f_c)$. Thus, for the cantilever alone, we have a delay time of $Q_c/(\pi f_c) + 1/(2f_c)$, when the cantilever oscillation amplitude can be measured at every half cycle of the oscillation. The value of this time delay is about 0.95 μs for our small cantilevers with f_c ~1.2 MHz and Q_c ~2 in water (vide Section 4.1).

3.2 Time delay with scanner

The response of z-scanner with the first resonant frequency f_z and a quality factor Q_z is characterized with a second-order transfer function. The phase delay φ_z at the feedback frequency f can be estimated from the phase-frequency relationship (*i.e.*, the Bode phase plot) of the transfer function. The time delay τ_z is given by $\tau_z = \varphi_z/(2\pi f)$. For our z-scanner with f_z = 370 kHz and the maximum displacement ~1 μm (vide Section 4.1), the phase delay is approximately 8.3° when driven at 100 kHz through an active damping circuit with a mock z-scanner constructed by an *LRC* circuit[17] (vide Section 4.4.2), and thus, τ_z ~0.23 μs. By active damping, the Q_z value is moderately suppressed to ~2 to avoid a large phase delay. The resonance at 370 kHz is not excited by driving at 100 kHz.

3.3 Time delay with parachuting

Other delay factors arise from electronic circuits contained in the feedback loop and from parachuting. Our analogue electronics circuits (a preamplifier and a signal conditioner used in the optical beam deflection (OBD) detector for measuring cantilever deflection, a piezodriver for z-scanner, and a PID controller) are minor delay factors. Parachuting is apt to occur frequently and prolonged when the cantilever amplitude set point A_s is set close to the free oscillation amplitude A_0 so that the oscillating tip lightly taps the sample. This issue is problematic and a major obstacle to making high-speed AFM imaging compatible with low-invasive imaging. The maximum set point r_{max} with which parachuting does not occurs can be obtained by the relationship $\Delta S(t) + A_0(1 - r_{max}) = 0$ and is expressed as

$$r_{max} = 1 - \frac{h_0}{A_0} sin \frac{\theta_{close}}{2}. \quad (4)$$

For example, when $h_0 = 2A_0$ and $r_{max} = 0.9$, we obtain $\theta_{close} = 5.7°$. This means that to avoid parachuting, we have to slow down the imaging rate so that feedback frequency f becomes much lower than the feedback bandwidth; *i.e.*, $f = \{\theta_{close}/(\pi/4)\}f_B \sim 0.13\ f_B$. In other words, when scanned at $f = f_B$, significant parachuting occurs and thus the most of downhill regions of the sample cannot be imaged at all. We have solved this difficult problem by inventing a new feedback controller termed "dynamic PID controller".[18] This controller makes low-invasive imaging possible without deterioration of the scan speed because it can completely suppress parachuting as far as the condition $A_s \leq 0.9 \times A_0$ is used (vide Section 4.4.3). Analytical expression of parachuting time (delay time) is given elsewhere.[16]

4. Components and Control Techniques for HS-AFM

As comprehensive descriptions of devices and techniques developed for HS-AFM are already given elsewhere,[16] only their outlines are described here. Our HS-AFM instrument is now commercialized by Research Institute of Biomolecule Metrology Co., Ltd. (Tsukuba, Japan).

4.1 Small cantilevers

Several types of small rectangular cantilevers made of silicon nitride have been developed by Olympus in collaboration with our group. The high-end small cantilevers (BL-AC7DS-KU2; custom-made by Olympus) which we have been routinely using for imaging studies are 6–7 μm long, 2 μm wide, and 90 nm thick (Fig. 4A). They have mechanical properties of f_c ~1.2 MHz in water (~3.5 MHz in air), Q_c ~ 2 in water, and a spring constant k_c ~0.2 N/m. The commercially available small cantilevers

(BL-AC10DS-A2, Olympus) are 9-10 μm long, 2 μm wide and 130 nm thick, and have f_c ~0.6 MHz in water (1.5 MHz in air), Q_c ~2 in water, and k_c ~0.1 N/m.

The change in the angle $\Delta\varphi$ of the free end of a cantilever is given by $\Delta\varphi = 3\Delta z/(2L)$, where Δz is vertical displacement of the free end and L is the cantilever length. For the short cantilevers, the angle-based OBD detection of cantilever deflection[7,8,35] is, therefore, advantageous, compared with distance-based detection, for example, by optical interferometric methods.[36,37] The short cantilevers grant 10–20-times higher sensitivity to the OBD detection than conventional cantilevers. We have been using an OBD detector optimized for small cantilevers.[8]

4.2 Cantilever tip

The tip of small cantilevers manufactured by Olympus has a bird-beak like shape with an apex radius 15–24 nm (Fig. 4A).[10] Therefore, we have to attach a sharper tip to the bird-beak tip in order to obtain high-resolution images. Although attaching[38,39] or directly growing[40] a thin carbon nanotube to an original cantilever tip is reported, their procedures are too demanding to use routinely. Using a scanning electron microscope (SEM; a low vacuum type), we routinely prepare electron beam deposited (EBD) tips under the atmosphere of phenol gas sublimated from phenol crystals (Fig. 4B, C).[16] They grow at ~1 μm/min under a low vacuum condition. The tip can be sharpened by nitrogen or oxygen plasma etching.[16] The apex radius is usually reduced to ~5 nm (Fig. 4D) and sometimes reduced to ~0.5 nm (yield ~ 10%), judging from AFM images obtained with the sharpened tips.[23] Since the tip radius directly influences the resolution of captured images, we need to improve our method to enhance the yield of sharp tips with an apex radius of ~0.5 nm. The reason for the low yield is due likely to that the

apex with ~0.5 nm radius produced during plasma etching tends to be collapsed by slight further etching.

Harder materials rather than carbon will probably produce sharp tips with a higher yield. Although we have not yet tried, we can prepare EBD tips of tungsten or a mixture of tungsten and carbon. A gas injection system, which is adaptable to SEMs and can mix different gasses under computer control, is commercially available (OmniGIS^{TM}, Omniprobe, Dallas, USA).

4.3 Fast amplitude detector

We developed two types of fast amplitude detectors; peak-hold and Fourier types (Fig. 5). The peak-hold type (Fig. 5A) holds the sinusoidal output from the split-photodiode sensor (quadrant PIN diode sensor) at its peak and bottom and outputs their difference as peak-to-peak amplitude at every half cycle of cantilever oscillation.[8)] The sample/hold timing signals are generated using either the split-photodiode sensor output itself (internal mode) or a signal synchronized with the cantilever excitation signal (external mode). In addition to decrease of the cantilever oscillation amplitude, the resonant frequency of the cantilever shifts towards a higher frequency when repulsive force acts on the tip. This frequency shift results in a phase shift of the cantilever oscillation relative to the excitation signal. Therefore, in the external mode where the sample/hold timings are independent of the phase shift, the detected amplitude signal is affected by the phase shift. Therefore, the external mode is more sensitive to the tip-sample interaction than the internal mode. Here, note that the phase shift of an oscillating small cantilever is ~1,000-times larger than that of conventional cantilevers because of the large resonant frequency-to-spring constant ratio of the small cantilevers.

Although this amplitude detection is fastest, it is apt to be affected by the thermal motion of the cantilever because only two-point voltages of the split-photodiode sensor output are used. In the Fourier type (Fig. 5B), the Fourier sine and cosine coefficients (a and b, respectively) are calculated for the cantilever's first resonant frequency component of the split-photodiode sensor signal and $(a^2 + b^2)^{1/2}$ is output at every cycle of cantilever oscillation.[16] This detector is less susceptive to the thermal effect (~1/4) than the peak-hold type.

4.4 High-speed scanner

Some conditions are required of the high-speed scanner; (a) high resonant frequency, (b) small number of resonant peaks within a narrow frequency range, (c) sufficient maximum displacement, (d) small crosstalk between the three scan axes, and (e) small quality factor. Here, several techniques that have met these conditions are described.

4.4.1 Mechanical design and counterbalance

The quick displacement of a piezoactuator exerts a large impulsive force to the supporting base, causing vibrations of the base and the surrounding mechanisms and in turn of the actuator itself. To alleviate the vibrations, counterbalance methods have been introduced to the x- and z-scanners (Fig. 6). For the z-scanner, two identical piezoactuators are attached to a supporting base at the counter planes.[16] Impulsive forces are countered by the simultaneous displacement of the actuators of the same length in the counter directions. In another method used for the z-scanner, a piezoactuator is held at the four rims parallel to the displacement direction so that its center of mass remains unchanged during displacement.[15] In this method, the maximum displacement becomes one half of that in the first method but the resonant frequency

remains almost unchanged from that in free oscillation. For the x-scanner, a piezoactuator is held at the two opposite planes (perpendicular to the displacement direction) with a pair of flexures so that the center of mass of the actuator remains unchanged during its displacement.[16] The y-scanner displaces a block containing the x- and z-scanners, the x-scanner displaces a block containing the z-scanner, and the z-scanner displaces a sample stage. Each block is connected with a surrounding mechanism through a pair of flexures. The flexures are flexible in the displacement directions but are stiff in the perpendicular directions. This connection between the x-, y-, and z-scanners through the flexures minimizes crosstalk between the three scan axes. The scanner's surrounding mechanism and flexures are monolithically fabricated from a stainless steel block or from a duralumin block. The gaps in the scanner are filled with an elastomer to passively damp the vibrations.

4.4.2 Active damping

The fast scanners designed as above have a small number of resonant peaks. The resonant peaks generally consist of the structural resonance (arising from the scanner mechanism) and the resonance of actuators themselves. The resonant peaks of the x-scanner are comprised of both types of resonances and the frequency of its structural resonance is lower than that of the x-piezoactuator itself. Both resonances can be simultaneously eliminated by a feedforward compensation method because it is scanned in a periodic pattern (isosceles triangle waveform).[16] Let's express the Fourier transform of a series of isosceles triangles as $F(\omega)$ and the transfer function of the x-scanner as $G(\omega)$. In the compensation method, the inverse Fourier transform of $F(\omega)/G(\omega)$ is calculated and output to the x-scanner driver through a D/A converter.

The first ~10 terms in the infinite series of the inverse Fourier transform are practically sufficient for driving the x-scanner in a well approximated isosceles triangle waveform. This method can extend the x-scanner bandwidth as far as the piezodriver to be used has a sufficient bandwidth for higher frequencies.

This feedforward method cannot be applied to the z-scanner because its displacement is not periodic and unspecified beforehand. When an alternative feedback method for damping is used, the displacement or speed of the z-scanner has to be measured but it is difficult to do so. We developed a feedback Q-control method in which the output from a "mock z-scanner" (*LRC* circuit) is used.[17] The mock z-scanner is characterized with a transfer function similar to that of the real z-scanner. An input signal to the z-piezodriver is also input to the mock z-scanner, and the minus derivative of the output from the mock z-scanner is added to the output signal from a PID feedback controller (Fig. 7). As a result, the quality factor Q_z is reduced.

4.4.3 Dynamic PID control and drift compensation

As shown in Fig. 3, the plus-minus sign of the error signal is different between the uphill and downhill regions of the sample. Therefore, the sign of error signal indicates which region is being scanned. We used this indicator to eliminate the tip parachuting effect. Simply, the feedback gain is increased for the downhill region while the gain is kept constant for the uphill region.[18] There are several ways to automatically change the feedback gain depending on the error signal (or on the cantilever oscillation amplitude). We employed the following method. A threshold level A_{upper} is set at (or slightly above) the amplitude set point A_s. When the cantilever oscillation amplitude A exceeds this threshold level, the differential signal ($A - A_{\mathrm{upper}}$) is amplified and added to the error

signal. The error signal that contains an extra signal is fed to the conventional PID controller. The “false error signal” which is larger than the “true error signal” produces a quicker feedback response, and therefore, A quickly becomes smaller than A_{upper} and the feedback operation automatically returns to the normal mode. Thus, even with A_s very close to A_0, the parachuting period is shortened drastically or can be completely eliminated.

To minimize the tapping force, cantilever free oscillation amplitude A_0 = 1 – 2 nm is used. Therefore, the difference between A_0 and A_s is very small (~0.1 – 0.2 nm) under the condition A_s ~0.9 × A_0. However, the oscillation power of an excitation piezoactuator gradually decreases with time because the excitation efficiency becomes low due probably to temperature rising of the piezo actuator. So, A_0 easily decreases by > 0.2 nm due to this drift, and therefore, stable imaging is difficult under this condition. This problem was solved by maintaining the constant average amplitude of a second harmonic oscillation of the cantilever by controlling the power driving the excitation piezoactuator.[18] This drift compensator enables stable low-invasive and high-speed imaging when operating together with the dynamic PID controller, even under the conditions of A_0 = 1 – 2 nm and A_s ~0.9 ×A_0.

5. Sample Stage and Hydrodynamic Pressure

In high-speed imaging, the sample-stage z-scanner moves at high frequencies (50 – 100 kHz) and hence a substrate, which is attached to a sample stage and in contact with a buffer solution, is also moves at high frequencies in the z-direction. This fast movement of the substrate produces a hydrodynamic pressure. An oscillating cantilever and its supporting base are positioned very close to the substrate surface (here, the supporting

base, which we call “wing” (Fig. 4E, F), means a portion that bridges the cantilever beam and the large base directly in contact with the cantilever holder). Therefore, they are apt to be moved by the hydrodynamic pressure particularly when the sample stage is large. The movement results in slow response of the cantilever oscillation amplitude to z-scanner displacement. Therefore, in a HS-AFM system with a sample-stage scanner rather than a tip-scanner, the size of sample stage should be minimized.[9] As a sample stage, we routinely use a glass rod of 1.5 - 2 mm in diameter and 2 mm in height to the upper end of which a substrate (usually a mica disk with 1mm diameter and < 0.1 mm thickness) is glued with epoxy adhesive. The bottom end of the glass rod is glued onto the top of the z-piezoactuator with nail enamel.

Further precautions are required for minimizing the hydrodynamic pressure effect. Even with a small sample stage, the hydrodynamic pressure is large at its central area. In fact, when a cantilever tip is placed at the central area and contacted with the substrate surface, the response of cantilever oscillation amplitude to quick displacement of the sample stage is delayed.[41] In the worst case, this delay extends to a few μs which is significantly longer than the minimized total time delay in the feedback loop. When the cantilever tip is placed at an edge region of the sample stage so that the whole cantilever chip is minimally overlapped with the sample stage, no time delay due to hydrodynamic pressure is observed. The angle between the top surface of the sample stage and a cantilever (the whole cantilever chip) is also an important factor. When the angle is small (~5°), the wing of the cantilever is apt to undergo the hydrodynamic pressure. We usually set the angle at ~10°.

The design of the wing is also an important factor for minimizing the hydrodynamic pressure effect. In a previous design, the wing is large (Fig. 4E) while it is much smaller

in the current one (Fig. 4F). The cantilevers with the latter design are much less affected by the hydrodynamic pressure. Unfortunately, this excellent improvement is not yet employed for the commercial small cantilevers produced by Olympus.

The shape and length of cantilever tip are also important factors to consider. When the tip is shorter, the cantilever gets closer to the sample surface at the bottom of swing and thus a solution confined between them is more squeezed, resulting in oscillation damping. This squeeze effect also occurs at the space confined by the tip and the sample surface when the tip is wider. Not only damping but also deterioration of sensitivity to the tip-sample interaction is caused by the squeeze effect. Fig. 8 shows force curves obtained using small cantilevers with different tip shapes and lengths. When the 1.5 μm long tip with bird-beak shape is used, the cantilever oscillation amplitude is getting smaller as approaching to the substrate surface, whereas when the tip has an additional 1 μm long needle-shaped tip, the oscillation amplitude is maintained constant until the tip comes into contact with the substrate surface. Moreover, when contacted with the surface, the oscillation amplitude more sharply decreases with the longer tip than with the shorter one.

6. Substrate Surfaces

A substrate surface, on which a sample is placed, plays an important role in dynamic AFM imaging. To observe dynamically acting protein molecules under physiological conditions, the substrate surface must have an appropriate affinity for the molecules. When the affinity is too low, protein molecules diffuse rapidly on the surface and cannot be clearly imaged even with HS-AFM. When the affinity is too high, the molecules often lose the biological function. To observe dynamic interactions between

different proteins, selective protein attachment to a surface is required. Otherwise, there is no chance of their interaction. Thus, we have to prepare an appropriate substrate surface depending on the dynamic biomolecular event to be visualized. As a substrate surface, bare[24, 26-28,32,33,42] or chemically treated[23] mica surfaces, planar lipid bilayer surfaces,[22] and the surfaces of two-dimensional crystals of streptavidin formed on a biotin-containing lipid bilayer have been used for dynamic AFM imaging.[34,43]

Mica (natural muscovite or synthetic fluorophlogopite) has been frequently used as substrate source due to its surface flatness at the atomic level over a large area. It has net negative charge and therefore is quite hydrophilic. A bare mica surface adsorbs various proteins by electrostatic interaction. We can control the affinity to a specific protein by varying the ionic strength or pH, or by adding divalent cations such as Mg^{2+}. For immobilization of fractionated membranes containing membrane proteins, the bare mica surface is most useful. A water-layer of thickness ~1 nm separates the membranes from the mica surface enabling motion of membrane proteins within the membranes.[44,45] In fact, bacteriorhodopsin (bR) in the non-crystalline region rapidly diffuses in the purple membrane attached to a bare mica surface.[27] By chemically treating a mica surface, proteins can be covalently immobilized onto the surface. For instance, F_1-ATPase was attached onto a mica surface in a selective orientation; the mica surface was first coated with amino silane and then treated with an amino crosslinker, glutaraldehyde. F_1-ATPase with $(Lys)_7$ introduced to the N-terminus of the α and β subunits was covalently immobilized onto the surface, in an end-up orientation with the C-terminal surface at the top.[23]

The surface of two-dimensional crystals of streptavidin is particularly useful for selective immobilization of homo-oligomeric protein complexes, such as GroEL and

actin filaments because stable pining of the complexes at multiple biotinylated sites is possible.[34,46] Importantly, the surface is resistant to non-specific binding of proteins. However, for non-oligomeric proteins, their tethering to the surface through a single biotinylated site sometimes results in rapid motion around the link. The high mobility can be reduced by using reactive dibiotin compounds.

Planar lipid bilayer surfaces can be used for both specific and non-specific (electrostatic) immobilization of proteins.[22,46] For specific immobilization of biotinylated proteins and His-tag conjugated proteins, lipids with biotin and Ni-NTA (nickel-nitrilotriacetic acid) at the polar head groups can be used, respectively. Multiple-point pining is sometimes required for stopping rapid motion of molecules tethered to the surface. Planar lipid bilayer surfaces prepared using electrically neutral phospholipids are very resistant to non-specific binding of proteins. For electrostatic immobilization, lipids with charged head groups can be used. Unlike bare mica surfaces, the surface charge density can be controlled by using different fractions of a charged lipid. The charge polarity can also be altered by using positively or negatively charged lipids. For dynamic AFM imaging of myosin V on an actin filament, a planar lipid bilayer surface comprised of a biotinylated lipid and positively and neutrally charged lipids was used.[22]

7. Imaging Studies

Around 2008, the instrumentation of HS-AFM was nearly matured, and thus, HS-AFM started to be used to solve biological issues that had been difficult or impossible to address with other methods. Since then, the number of publications on bio-imaging by HS-AFM gradually increased and rapidly increased in the last two years.

The imaging studies conducted thus far cover a wide range of dynamic molecular processes and structure dynamics; myosin V walking on an actin filament,[22] rotary catalysis of rotorless F_1-ATPase,[23] bacteriorhodopsin in response to light,[24,26] dynamics of bacteriorhodopsin 2D crystals,[27,28] ATP-induced structural changes in $P2X_4$ receptors,[29] cellulase hydrolyzing cellulose fibers,[30,31] amyloid-like fibril formation from cleaved lithostathine,[32] formation of supported planar lipid bilayers,[47] reaction of DNA restriction-modification enzyme,[48,49] unwrapping of nucleosomes,[50,51] GroEL-GroES interaction regulated by ATP hydrolysis by GroEL,[14,34,52] undulation motion of an intrinsically disordered protein[42], membrane-mediated interaction between c-rings of ATP synthase,[33] collapse of three-dimensional DNA origamis,[53,54] defects diffusion in protein 2D crystals,[43] enzymatic reactions on DNA origamis,[55,56] translocation of a DNA nanorobot on a track formed on a DNA origami tile,[57] and so on. Moreover, non-biological dynamic phenomena, such as photodegradation of single chains of a chiral helical π-conjugated polymer,[58] phase transition of detergent aggregates,[59] and photoresists dissolution,[60] are also studied. Georg Fantner studied kinetics of antimicrobial peptide-induced morphological change in individual bacterial cells using a HS-AFM instrument and small cantilevers he developed.[61] In this Section, some of imaging studies performed by our group are highlighted. Several molecular movies can be seen at our home page http://www.s.kanazawa-u.ac.jp/phys/biophys/index.htm.

7.1 Bacteriorhodopsin in response to light

Bacteriorhodopsin (bR) functions as a light-driven proton pump, transferring protons across the membrane from the cytoplasmic side to the extracellular side.[62,63] bR is

comprised of seven transmembrane α-helices (named A-G) surrounding the retinal chromophore covalently bound to Lys216 via a protonated Schiff base.[64,65] In the purple membrane, bR assembles into trimers, and the trimers are arranged in a hexagonal lattice. Upon absorption of light, photoisomerization from all-*trans* to 13-*cis* conformation of the retinal takes place. This isomerization induces proton transfer from the Schiff base to Asp85, which triggers a cascade of changes in the bR structure. A series of intermediates designated J, K, L, M, N, and O are defined by spectroscopy, and M (M_{410}), which has an absorption peak at 410 nm and the longest lifetime, is only the intermediate containing a deprotonated Schiff base.[63] The light-induced conformational changes in bR in the frozen activated state of the wild type (WT) and bR mutants have been studied by x-ray crystallography and electron microscopy.[66-68] The extent of the changes reported varies depending on the methods used but is generally small (0.1 − 0.3 nm). Until our recent study, dynamic nature of the conformational changes has, however, been remained elusive due to the lack of techniques amenable to the high-resolution visualization of dynamic structural changes of proteins. Our group for the first time succeeded in capturing high-resolution successive images showing dynamic changes of bR in response to light using HS-AFM.[24,26]

The photocycle of the wild type at neutral pH proceeds very fast (~10 ms). To slow down the photocycle, we then used the D96N bR mutant that has a longer photocycle (~10 s at pH 7) but still retains an ability of proton pumping.[69] The native purple membranes containing D96N bR were directly placed on a bare mica surface. Fig. 9A presents successive images of D96N mutant at the cytoplasmic surface captured at 1 fps. Upon illumination with green light (532 nm, 0.5 μW), bR drastically changed its structure (compare images at 1 and 2 s) and returned to the unphotolysed state in a few

seconds after light-off. Note that this structural change is specifically induced by green light not by blue or red light and that bR in the ground state effectively absorbs green light. All the activated bR monomers moved outwards by 0.7 − 0.8 nm from the centers of respective trimers and rotated counterclockwise by 7 − 8° around the centers of respective trimers, as illustrated by arrows in Fig 9B. However, the overall position of each bR molecule does not change because of indiscernible alterations at the extracellular surface. The photo-activated state observed by high-speed AFM could be attributed to the spectroscopically identified M intermediate because the lifetimes of other spectroscopic intermediates occurring prior M are very short. However, it was uncertain whether the photoactivated state detected by AFM also contained the N intermediate that follows M. This issue was solved in our further study.[26)] In this study, the D96N mutants were alternatively illuminated by green and blue light. It is well known that absorption of blue light by retinal in M_{410} induces back isomerisation reaction of the retinal. The HS-AFM observation showed that the bR molecules activated by green light illumination quickly return back to the ground state upon subsequent blue light illumination. This means that the excited state detected by HS-AFM only contains the M intermediate. Moreover, it was also revealed by this observation that the conformation of bR is tightly governed by the conformation of retinal.

As a result of the outward displacement, nearest-neighbor bR monomers, each belonging to a different adjacent trimer, transiently assemble, as illustrated in Fig. 9C. Here, we use a new designation, ‘trefoil’, for the triad of nearest-neighbor monomers belonging to different trimers to distinguish it from the original trimer. To investigate a possible effect of bR-bR interaction within a trefoil on the photocycle, bR was

illuminated with different light intensities (0.007 – 0.5 μW). Under weak illumination, only one monomer in each trefoil was activated in the most cases. When only one monomer was activated in a trefoil, it decayed with a time constant of 7.3 ± 0.58 s. In contrast, under stronger illumination, two or three monomers within a trefoil tended to be activated together. Interestingly, the decay of each monomer markedly depended on the order of its activation. The monomer that was activated latest among the activated monomers in a trefoil decayed with a shorter time constant of 2.0 ± 0.16 s. On the other hand, the decay kinetics of the early activated monomers did not follow a single exponential, and the averaged decay time lengthened to ~13 s. This observation indicates that the early activated monomers do not return to the ground state as long as the adjacent monomers within the trefoil are in the active state. Thus, bR-bR interaction within a trefoil under illumination engenders both positive and negative cooperative effects in the decay kinetics as the initial bR recovers. It is interesting that the cooperativity does not occur within a trimer but within a trefoil. As a consequence of both positive and negative cooperative effects, the turnover rate of the photocycle is maintained constant, on average, irrespective of the light intensity. This seems to indicate the reason why bR trimers assemble into a hexagonal lattice in the native state

7.2 Cellulase Hydrolyzing Cellulose Fibers

Cellulose is the most abundant biomass and component of feed crops used in livestock industry. Therefore, the efficient conversion of cellulose to fuels and the improvement of cellulose digestibility particularly for ruminants are important issues in agricultural industries. One of the problems in biorefining applications to cellulose is the low enzymatic hydrolysis of cellulosic raw materials. To maximize the hydrolysis efficiency,

various studies have been carried out on individual cellulases, cellulase cocktails,[70] and pretreatment of cellulose fibers. One of the most serious problems is that the rate of hydrolysis is quickly slowed down with time in an uncertain mechanism.[71,72] Biochemical analyses are ineffective for this issue because the reaction occurs not in a bulk solution but on a solid-liquid interface. We attempted to find the mechanism by observing cellulase molecules hydrolyzing cellulose fibers using HS-AFM.[31] This approach was demonstrated to be effective for such a unique enzymatic reaction.

7.2.1 Traffic jam of cellulase on cellulose fibers

The cellulolytic ascomycete fungus *Trichoderma reesei* (*Tr*) secretes two extracellular cellulases *Tr*Cel7A and *Tr*Cel6A that hydrolyze glycosidic linkages of crystalline cellulose to produce cellobiose (β-1,4-glucose dimmer).[73] *Tr*Cel7A hydrolyzes cellulose from its reducing end while *Tr*Cel6A does from the non-reducing end.[74] These enzymes have a similar two-domain structure (Fig. 10A); a small cellulose-binding domain (CBD) and a larger catalytic domain (CD). The active site is located in a relatively long tunnel formed in CD; 5 nm long in the case of *Tr*Cel7A and 2 nm long in the case of *Tr*Cel6A.[75,76] Therefore, these enzymes has been thought to consecutively hydrolyze a crystalline cellulose chain without releasing the chain, and thus, expected to processively and unidirectionally move along a cellulose fiber.[73-77]

Crystalline cellulose I_α was placed on a bare surface of highly ordered pyrolytic graphite (HOPG) and *Tr*Cel7A was added in the bulk solution. As shown in Fig. 10B, *Tr*Cel7A, in fact, moved processively and unidirectionally on the surface of crystalline cellulose.[30,31] The unidirectional movement of *Tr*Cel7A was not smooth but intermittently repeated stop and go behaviors (Fig. 10C). When it continuously moved

within a certain range, its velocity was 7.1 nm/s on average. The overall averaged speed was 5.3 nm/s, without considering molecules which were completely halted during imaging. One hydrolytic cycle produces one cellobiose unit of approximately 1 nm in length. Therefore, the hydrolysis rate is estimated to be ~5/s. This value is about 300 times higher than the biochemically measured hydrolysis rate. This large discrepancy seems due mainly to the limited number of available reduced ends in the crystalline cellulose.

Crystalline cellulose III_I, which has a crystalline polymorphic form different from that of cellulose I_α, is formed through super-critical ammonium treatment of cellulose I_α and can be more effectively degraded by *Tr*Cel7A.[78)] A biochemical analysis indicated that *Tr*Cel7A has a higher affinity for cellulose III_I than for cellulose I_α but its maximum hydrolysis rate is only slightly higher than cellulose I_α.[78)] The HS-AFM observation of *Tr*Cel7A movement on the surface of cellulose III_I revealed a “traffic jam” of bound enzyme molecules (Fig. 10D). When one molecule was halted, many following molecules stacked behind it, causing a traffic jam. However, after additional molecules had also become blocked, the enzyme molecules restarted to move again on the surface, and a cellulose bundle was peeled off from the crystalline cellulose (Fig. 10E). These phenomena of traffic jam and fiber peeling may be able to account for the rapid retardation of cellulose hydrolysis rate with time. The distance between neighboring traffic lanes is smaller than the size of *Tr*Cel7A. Therefore, the enzyme molecules moving along neighboring lanes have a large chance to collide with each other. Before adding *Tr*Cel7A, the surface of crystalline cellulose fibers is smooth. When a *Tr*Cel7A molecule is hydrolyzing one lane of cellulose, it is likely that the molecule partially peels lanes adjacent to the lane being hydrolyzed by the molecule. This peeling is likely

to result in the go and stop behavior of the molecule as well as in a rough surface of crystalline cellulose, and thus, *Tr*Cel7A molecules are apt to be halted. Once one molecule is stacked, many molecules around it are also stacked. Most likely, this is the mechanism underlying the rapid retardation of cellulose hydrolysis rate.

7.2.2 Endo-exo synergy

As reported previously,[74,79] a cocktail of *Tr*Cel7A and *Tr*Cel6A synergistically increases the rate of cellobiose production (Fig. 11A). This effect seems peculiar because cellulose hydrolysis from both reducing and non-reducing ends cannot explain the synergy. To understand the mechanism underlying this synergistic effect, the cellulose degradation process was imaged first in the presence of *Tr*Cel6A alone. After a while, *Tr*Cel7A was added while imaging was continued. When *Tr*Cel6A was alone, no significant change was observed in the appearance of cellulose III_I microfibrils even 8 min after the addition of *Tr*Cel6A (although an image at 3.6 min is shown in Fig. 11B, the appearance was almost unchanged even at 8 min). However, the addition of *Tr*Cel7A at 8.3 min abruptly altered the microfibril appearance; the cellulose fibrils were being quickly degraded and almost completely disappeared at 3.6 min after the addition of *Tr*Cel7A (Fig. 11C). This observed synergistic effect was much more drastic than the biochemically observed one and was independent of the order of addition of the two enzymes. We noticed that bound *Tr*Cel6A molecules often detached from cellulose III_I without showing appreciable processive run. This fact and the observed synergy suggest that *Tr*Cel6A can also work as an endo-glucanase. The short active site tunnel of *Tr*Cel6A may be able to open and allow generation of nicks in the middle of crystalline cellulose, and therefore, these nicks become starting and ending points for

*Tr*Cel7A activity. Thus, the synergy observed is not exo-exo synergy but endo-exo one.

7.3 Walking Myosin V on Actin Filament

Double-headed myosin V (M5), which is a member of myosin super-family and functions as a cargo transporter in cells, has been extensively studied by single-molecule fluorescence microscopy and optical-trap namometry.[80] It moves processively along an actin filament towards the plus end of the filament[81,82] in a hand-over-hand manner with a 36-nm advance[83-85] for every ATP hydrolysis cycle.[86] "Hand-over-hand" means that the two heads step alternately exchanging leading and trailing roles at each step, very much like "walking". Nevertheless, comprehensive descriptions of the walking behavior and how force generation is coupled with the ATPase reaction have not been attained until our recent HS-AFM observation of the motor.[22]

7.3.1 Step motion of myosin V

To observe moving M5 molecules on actin filaments, the filaments have to be immobilized on a surface while M5 should be free from the surface. So, selective immobilization is required. As a substrate surface, we first used an electrically neutral phospholipid bilayer surface containing biotin-lipid, formed on mica. Partially biotinylated actin filaments were immobilized onto this surface through streptavidin with a low surface density. Tail-truncated M5 (M5-HMM) was never bound to this surface. Although these conditions are ideal, we then included a positively charged lipid 1,2-dipalmitoyl-3-trimethylammonium-propane (DPTAP, 5%) in the bilayer. The appropriately charged surface facilitated observing the sideways figure of actin-bound

M5-HMM. M5-HMM moving processively with ~36 nm steps was clearly visualized at 7 fps (Fig. 12A). The two-headed bound M5-HMM showed unique structural features (illustrated in Fig. 12B); the neck–motor domain junction appears smooth in the leading head but is V-shaped in the trailing head without exception, because the neck regions emerge from different parts of the motor domain (Fig. 12A, B). The short coiled-coil tail was mostly tilted towards the minus end of actin. These features can be used to determine the actin polarity when bound M5-HMM is stationary. When DPTAP was absent in the lipid bilayer, the average translocation velocity was similar to that measured by fluorescence microscopy under the same solution condition, indicating no effect of the tip-sample interaction on the motor activity. However, we could not see detailed molecular behavior during a step as it completed within a frame.

To slow down the step, streptavidin molecules were further placed on the substrate surface as moderate obstacles to the advance. This method allowed visualization of stepping processes (Fig. 12C; illustrated in Fig. 12D). After trailing head detachment, the leading head appeared to spontaneously rotate from the reverse arrowhead orientation towards the arrowhead orientation (the term “arrowhead” originates from the configuration of single headed myosin bound to an actin filament in the rigor state). Before completing this rotation, the leading head was halted for a while by colliding with a streptavidin molecule placed on the way of its natural path. In this halted state, the detached trailing head was most distant from the actin filament (thus, the two heads were aligned nearly straight, pointing opposite directions) and slightly rotated around the neck-neck junction (the second frame in Fig. 12C). Then, the leading head overcame the streptavidin blockade and completely rotated to the arrowhead orientation. Accompanied by this further rotation, the trailing head bound to a forward site of the

actin filament to become a new leading head, completing one step. Here, it was clearly revealed that during and before completing a step, the trailing head never interacts with actin and hence passively moves forwards, driven by the rotating leading head. Thus, the 'inchworm' mechanism (a molecule moves forward like inchworm in which one head always leads while the other head follows.) considered for kinesin[87] as well as 'biased diffusion' mechanism (a molecule moves forward by directional diffusion according to a potential slope created along the actin helix.) proposed for M5[88] can be ruled out. The rotation of the leading head is the swinging leverarm motion itself initially proposed by Hugh Huxley for the powerstroke of muscle myosin.[89]

7.3.2 Tension generation

The seemingly spontaneous rotation of leading head following trailing head detachment suggests that intramolecular tension for the advance has already existed in the two-headed bound molecule. In this bound state, the trailing head is in the arrowhead orientation. This orientation is natural one at least for the ADP-bound or nucleotide-free head, and hence, the intramolecular tension is not produced by the bound trailing head. On the other hand, the leading head is not in the natural orientation (*i.e.*, in the reverse arrowhead orientation) and hence pays energy cost to generate the intramolecular tension. In fact, the bound leading head is slightly curved outwards while the trailing head is straight (Fig. 12A, B). Upon trailing head detachment, the constraint keeping the bound leading head in the unnatural orientation is removed and hence the leading head spontaneously rotates forwards, meaning that the bound leading head is in the strained pre-stroke state and the leverarm swing is not accompanied by chemical transitions.

This inferred view was reinforced by the observation that the short coiled-coil of two-headed bound M5-HMM was sometimes unfolded and then the leading head rotated from the reverse arrowhead orientation to the arrowhead orientation, very much similar to the swinging leverarm motion observed during a step (Fig. 13A). The uncoiling is caused by the intramolecular tension, not by the interaction with the oscillating cantilever tip. This is suggested by the fact that a fraction of single-headed species is contained in the sample of M5-HMM purified through actin binding and dissociation.[90)]

In general, during the actomyosin ATPase cycle, the strained pre-stroke state has been thought to be always formed through Pi release from an ADP-Pi bound head weakly interacting with actin.[91,92)] Thus, it may be considered that the strained pre-stroke state, which is formed directly by the binding of ADP-bound leading head to actin, does not participate in the forward step in ATP. However, we observed molecular behavior in ATP that indicates that it does participate. In two-headed bound M5-HMM, both of the motor domains frequently exhibited brief dissociation and reassociation on the same actin filament (or a brief translocation by around ± 5nm along the actin filament), whereas M5-HMM remained at approximately the same position on the filament (Fig. 13B). We have termed this behavior “foot stomp”. The foot stomp was more frequently observed at the leading head than at the trailing head. The briefly detached leading head does not carry bound Pi because Pi must have been released from an ADP-Pi-bound M5 head when it is initially bound to actin.[93)] This rapid Pi release is a general feature of actomyosin ATPase reaction. Nevertheless, the detached leading head with only ADP bound rebinds to actin, still in the reverse arrowhead orientation, and then swings forward following trailing head detachment.

The detachment of leading head during foot stomp is not caused by ATP binding to the leading head. As described in the next section, a nucleotide-free leading head is often sharply bent. We never observed a sharply bent leading head before foot stomp.

7.3.3 Mechanism of hand-over-hand movement

The leading head of two-headed bound M5-HMM was straight (slightly curved outwards) in ADP or ATP, while it was often sharply bent in the nucleotide-free condition (Fig. 13C). Therefore, just by looking at the conformation of leading head, we can judge whether or not the leading head contains nucleotides. To estimate the ADP dissociation rate constant at the leading head, M5-HMM bound to actin in various concentrations of ADP was observed, and then, the lifetime of straight leading head was analyzed as a function of ADP concentration. The ADP dissociation rate constant at the leading head was estimated to be 0.1/s. This means that ADP is released from the leading head every 10 s, on average. However, M5-HMM walks many steps for 10 s, meaning that ADP does not dissociate from the leading head. That is, before ADP dissociation from the leading head, the leading head is switched to the trailing head during walking. ADP dissociation, the subsequent ATP binding, and the resulting detachment from actin solely occurs at the trailing head. This is the basis underlying the processive hand-over-hand movement. This mechanism was inferred previously from various indirect experiments[86,94-98] but is now clearly and directly demonstrated by the high-speed AFM observation.

7.4 Summary of imaging studies

As demonstrated in the three imaging studies highlighted above, HS-AFM imaging of proteins in action is a powerful approach to revealing how proteins operate to function.

Although only from one direction, the whole figure of a protein molecule and its minute change with time appear in an AFM movie. Unlike fluorescence microscopy, various dynamic events of a molecule appear in a molecular movie without planned selection, meaning that both expected and unexpected dynamic molecular behaviors can appear simultaneously. Therefore, we can have a great chance of learning several facts of molecular action in one imaging experiment. Moreover, molecular action appeared on video can often be interpreted straightforward without sophisticated analysis, leading to attainment of convincing and irrefutable conclusions. These general excellent features of HS-AFM imaging significantly facilitate and accelerate our understanding of the functional mechanism of proteins.

8. Outlook

Continued studies on a wide range of interesting dynamics of purified biological molecules will be more and more carried out using HS-AFM. HS-AFM will be used routinely in the near future, similarly to the path of conventional AFM. However, we need to explore dynamic events occurring not only with purified molecules but also with those on live cell membranes and organelles.

The membranes of live eukaryotic cells are extremely soft, and hence, largely deformed by the contact with a cantilever tip before appreciable deflection of the cantilever is detected. So, at present, it is impossible to image molecules on the membranes using AFM. However, the membranes of live bacterial cells and the outer surfaces of organelles such as mitochondria and nuclei are rather rigid. Nonetheless, molecular architectures on these surfaces have not been studied much using AFM. We can only find a few examples of such imaging studies; e.g., nuclear pore complexes on a

nuclear envelop[99,100], the hexagonal S-layer on the surface of *Corynebacterium glutamicum*,[101] and peptideglycan organization on the surface of *Lactococcus lactis*.[102] Since dynamic molecular events occurring on these surfaces are largely unknown, it is worthwhile to attempt to image them using HS-AFM. This direction of studies will be more actively performed.

As mentioned above, the membranes of live eukaryotic cells are extremely soft. This is due to the wide area of the membranes. For small structures, such as dendritic spines (~0.5 μm in diameter) where most excitatory synapses reside, we may be able to visualize individual proteins on their surfaces. Even without molecular resolution, observing dynamic morphological changes in such cellular structures are intriguing and meaningful because of their inaccessibility from other approaches. For example, spine enlargement associated with long-term synaptic potentiation,[103,104] a cellular model for learning and memory, takes place together with exocytosis and endocytosis of vesicles.[105-107] However, the detailed dynamics of membrane trafficking during spine growth are unknown.

To visualize molecules on large eukaryotic cell surfaces, we need non-contact condition. The noncontact imaging capability in liquids has already been achieved by scanning ion-conductance microscopy (SICM).[108] Owing to the progress of fabrication techniques for producing very sharp glass capillaries with a small pore at the apex, the spatial resolution of SICM has reached a few nm.[109] Immobile protein molecules with a size of ~14 nm on living cell membranes have been successfully imaged.[110] Moreover, hopping-mode SICM, which is similar to a previously developed AC-mode SICM,[111] is recently devised to avoid collision of the capillary electrode probe with tall samples.[111] However, the bandwidth of ion-conductance detection cannot easily be increased,

because of the high impedance to ionic current through the small pore of the capillary electrode as well as slow ionic currents in aqueous solutions. Nevertheless, we believe that to increase the bandwidth is not impossible. Scanning tunneling microscopy has the high impedance problem but it has been overcome.[113] By adapting the high-speed scanning setup based on fast scanner and control techniques achieved in HS-AFM, various types of high-speed scanning probe microscopy techniques including high-speed SICM will be developed in the future as innovative tools for biological research.

Acknowledgements

We would like to thank Daisuke Yamamoto, Hayato Yamashita, Mikihiro Shibata, Ryota Iino, Hiroyuki Noji, Kiyohiko Igarashi, Hideki Kandori, and present and previous many students in our lab for collaborations or discussions on topics we described in this review. Long-term financial support by NEDO, JST (CREST project), JSPS (Grant-in-Aid for Basic Research (S)), Knowledge Cluster Initiative, and the Mitsubishi Foundation is gratefully acknowledged.

References

1) C. Joo, H. Balci, Y. Ishitsuka, C. Buranachai, and T. Ha**:** Annu. Rev. Biochem. **77** (2008) 51.
2) H. Park, E. Toprak, and P. R. Selvin: Quat. Rev. Biophys. **40** (2007) 87.
3) G. Binnig, C. F. Quate, and Ch. Gerber: Phys. Rev. Lett. **56** (1986) 930.
4) S. Gould, O. Marti, B. Drake, L. Hellemans, C.E. Bracker, P.K. Hansma, N.L. Keder, M.M. Eddy, and G.D. Stucky**:** Nature **332** (1988) 332.

5) D. A. Walters, J. P. Cleveland, N. H. Thomson, P. K. Hansma**,** M. A. Wendman, G. Gurley, and V. Elings: Rev. Sci. Instrum. **67** (1996) 3583.

6) T. E. Schäffer, J. P. Cleveland, F. Ohnesorge, D. A. Walters, and P. K. Hansma: J. Appl. Phys. **80** (1996) 3622.

7) M. B. Viani, T. E. Schäffer, G. T. Paloczi, L .I. Pietrasanta, B. L. Smith, J. B. Thompson, M. Richter, M. Rief, H. E. Gaub, K. W. Plaxco, A. N. Cleland, H. G. Hansma, and P. K. Hansma: Rev. Sci. Instrum. **70** (1999) 4300.

8) T. Ando, N. Kodera, E. Takai, D. Maruyama, K. Saito, and A. Toda: Proc. Natl. Acad. Sci. USA **98** (2001) 12468.

9) T. Ando, N. Kodera, D. Maruyama, E. Takai, K. Saito, and A. Toda: Jpn. J. Appl. Phys. **41** (2002) 4851.

10) M. Kitazawa, K. Shiotani, and A. Toda: Jpn. J. Appl. Phys. **42** (2003) 4844.

11) J. H. Kindt, G. E. Fantner, J. A. Cutroni, and P. K. Hansma: Ultramicroscopy **100** (2004) 259.

12) G. E. Fantner, P. Hegarty, J. H. Kindt, G. Schitter, G. A. G. Cidade, and P. K. Hansma: Rev. Sci. Insturm. **76** (2005) 026118.

13) G. E. Fantner, G. Schitter, J. H. Kindt, T. Ivanov, K. Ivanova, R. Patel, N. Holten-Andersen, J. Adams, P. J. Thurner, I. W. Rangelow, and P. K. Hansma: Ultramicroscopy **106** (2006) 881.

14) T. Ando, T. Uchihashi, N. Kodera, A. Miyagi, R. Nakakita, H. Yamashita, and K. Matada: e-J. Surf. Sci. Nanotechnol. **3** (2005) 384.

15) T. Fukuma, Y. Okazaki, N. Kodera, T. Uchihashi, and T. Ando: Appl. Phys. Lett.

92 (2008) 243119.

16) T. Ando, T. Uchihashi, and T. Fukuma: Prog. Surf. Sci. **83** (2008) 337.

17) N. Kodera, H. Yamashita, and T. Ando: Rev. Sci. Instrum. **76** (2005) 053708.

18) N. Kodera, M. Sakashita, and T. Ando: Rev. Sci. Instrum. 77 (2006) 083704.

19) T. Uchihashi, N. Kodera, H. Itoh, H. Yamashita, and T. Ando: Jpn. J. Appl. Phys. **45** (2006) 1904.

20) T. Ando, T. Uchihashi, N. Kodera, A. Miyagi, R. Nakakita, H. Yamashita, and M. Sakashita: Jpn. J. Appl. Phys. **45** (2006) 1897.

21) T. Uchihashi, H. Yamashita, and T. Ando: Appl. Phys. Lett. **89** (2006) 213112.

22) N. Kodera, D. Yamamoto, R. Ishikawa, and T. Ando: Nature **468** (2010) 72.

23) T. Uchihashi, R. Iino, T. Ando, and H. Noji: *Science* **333** (2011) 755.

24) M. Shibata, H. Yamashita, T. Uchihashi, H. Kandori, and T. Ando: Nat. Nanotechnol. **5** (2010) 208.

25) T. R. Rodríguez, and R. García: Appl. Phys. Lett. **82**, (2003) 4821.

26) M. Shibata, T. Uchihashi, H. Yamashita, H. Kandori, and T. Ando: Angew. Chem. Int. ed. **50** (2011) 4410.

27) H. Yamashita, K. Voïtchovsky, T. Uchihashi, S. Antoranz Contera, J. F. Ryan, and T. Ando: J. Struct. Biol. **167** (2009) 153.

28) I. Casuso, N. Kodera, Ch. Le Grimellec, T. Ando, and S. Scheuring: Biophys J. 97 (2009) 1354.

29) Y. Shinozaki, K. Sumitomo, M. Tsuda, S. Koizumi, K. Inoue, and K. Torimitsu: PLoS Biol. **7** (2009) e1000103.

30) K. Igarashi, A. Koivula, M. Wada, S. Kimura, M. Penttilä, and M. Samejima: J. Biol. Chem. 284 (2009) 36186.

31) K. Igarashi, T. Uchihashi, A. Koivula, M. Wada, S. Kimura, T. Okamoto, M. Penttilä, T. Ando, and M. Samejima: *Science* **333** (2011) 1279.

32) P.-E. Milhiet, D. Yamamoto, O. Berthoumieu, P. Dosset, Ch. Le Grimellec, J.-M. Verdier, S. Marchal, and T. Ando: PLoS One **5** (2011) e13240.

33) I. Casuso, P. Sens, F. Rico, and S. Scheuring: Biophys. J. **99** (2010) L47.

34) D. Yamamoto, N. Nagura, S. Omote, M. Taniguchi, and T. Ando: Biophys. J. **97** (2009) 2358.

35) G. Meyer and N. M. Amer: Appl. Phys. Lett. **53** (1988) 1045.

36) Y, Martin, C. C. Williams, and H. K. Wickramasinghe: J. Appl. Phys. **61** (1987) 4723.

37) B. W. Hoogenboom, P. L. T. M. Frederix, J. L. Yang, S. Martin, Y. Pellmont, M. Steinacher, S. Zäch, E. Langenbach, H.-J. Heimbeck, A. Engel, and H. J. Hug: Appl. Phys. Lett. **86** (2005) 074101.

38) H. Nisijima, S. Kamo, S. Akita, Y. Nakayama, K. I. Hohmura, S. H. Yoshimura, and K. Takeyasu: Appl. Phys. Lett. **74** (1999) 4061.

39) S. P. Jarvis, T. Uchihashi, T. Ishida, H. Tokumoto, and Y. Nakayama: J. Phys. Chem. B **104** (2000) 6091.

40) C. L. Cheung, J. H. Hafner, and C. M. Lieber: Proc. Natl. Acad. Sci. USA **97** (2000) 3809.

41) T. Ando and T. Uchihashi: in Nanoscale liquid interfaces (Ed., T. Ondarçuhu and J.-P. Aimé), Pan Stanford Publishing, Singapore, **2011** (in press).

42) A. Miyagi, Y. Tsunaka, T. Uchihashi, K. Mayanagi, S. Hirose, K. Morikawa, and T. Ando: Chem. Phys. Chem. **9** (2008) 1859.

43) D. Yamamoto, T. Uchihashi, N. Kodera, and T. Ando: Nanotechnology **19** (2008) 384009.

44) E. Sackmann: Science 271 (1996) 43.

45) J. Kim, G. Kim, and P. S. Cremer: Langmuir 17 (2001) 7255.

46) D. Yamamoto, T. Uchihashi, N. Kodera, H. Yamashita, S. Nishikori, T. Ogura, M. Shibata, and T. Ando: Methods Enzymol. **475 B** (2010) 541.

47) M.-C. Giocondi, D. Yamamoto, E. Lesniewska, P.-E. Milhiet, T. Ando, and Ch. Le Grimellec: Biochim. Biophys. Acta.-Biomembrane **1798** (2010) 703.

48) N. Crampton, M. Yokokawa, D. T. F. Dryden, J. M. Edwardson, D. N. Rao, K. Takeyasu, S. H. Yshimura, and R. M. Henderson: Proc.Natl. Acad. Sci. USA **104** (2007) 12755.

49) H. Sugasawa, Y. Sugiyama, T. Morii, and T. Okada: Jpn. J. Appl. Phys. **47** (2008) 6168.

50) J. L. Gilmore, Y. Suzuki, G. Tamulaitis, V. Siksnys, K. Takeyasu, and Y. L. Lyubchenko: Biochemistry 48 (2009) 10492.

51) Y. Suzuki, Y. Higuchi, K. Hizume, M. Yokokawa, S. H. Yoshimura, K. Yoshikawa, and K. Takeyasu: Ultramicroscopy **110** (2010) 682.

52) M. Yokokawa, C. Wada, T. Ando, N. Sakai, A. Yagi, S. H. Yoshimura, and K. Takeyasu: EMBO J. **25** (2006) 4567.

53) F. Tanaka, T. Mochizuki, X. Liang, H. Asanuma, S. Tanaka, K. Suzuki, S. Kitamura, A. Nishikawa, K. Ui-Tei, and M. Hagiya: Nano Lett. **10** (2010) 3560.

54) M. Endo, K. Hidaka, and H. Sugiyama: Biomol. Chem. **9** (2011) 2075.

55) Y. Sannohe, M. Endo, Y. Katsuda, K. Hidaka, and H. Sugiyama: J. Am. Chem. Soc. **132** (2010) 16311.

56) M. Endo, Y. Katsuda, K. Hidaka, and H. Sugiyama: J. Am. Chem. Soc. **132** (2010) 1592.

57) F. J. S. Wickham, M. Endo, Y. Katsuda, K. Hidaka, J. Bath, H. Sugiyama, and A. J. Turberfield: Nat. Nanotechnol. **6** (2011) 166.

58) K. Shinohara, N. Kodera, and T. Oohashi: J. Polym. Sc.: Part A: Polym. Chem. **48** (2010) 4103.

59) S. Inoue, T. Uchihashi, D. Yamamoto, and T. Ando: Chem. Commun. **47** (2011) 4974.

60) T. Itani, and J. J. Santillan: Appl. Phys. Express **3** (2010) 061601.

61) G. E. Fantner, R. J. Barbero, D. S. Gray, and A. M. Belcher: Nat. Nanotechnol. **5** (2010) 280.

62) U. Haupts, J. Tittor, and D. Oesterhelt: Annu. Rev. Biophys. Biomol. Struct. **28** (1999) 367.

63) J. K. Lanyi: Annu. Rev. Physiol. **66** (2004) 665.

64) Y. Kimura, D. G. Vassylyev, A. Miyazawa, A. Kidera, M. Matsushima, K. Mitsuoka, K. Murata, T. Hirai, and Y. Fujiyoshi: Nature **389** (1997) 206.

65) H. Luecke, B. Schobert, H. T. Richter, J. P. Cartailler, and J. K. Lanyi: J. Mol. Biol. **291** (1999) 899.

66) H. Luecke, B. Schobert, J. K. Lanyi, E. N. Spudich, and J. L. Spudich: Science **293** (2001) 1499.

67) H. J. Sass, G. Buldt, R. Gessenich, D. Hen, D. Neff, R. Schleisinger, J. Berendzen, and P. Ormos: Nature **406** (2000) 649.

68) S. Subramaniam and R. Henderson: Nature **406** (2000) 653.

69) H. Otto, T. Marti, M. Holz, T. Mogi, M. Lindau, H. G. Khorana, and M. P. Heyn:

Proc. Natl Acad. Sci. USA **86** (1989) 9228.

70) M. E. Himmel, S.-Y. Ding, D. K. Johnson, W. S. Adney, M. R. Nimlos, J. W. Brady, and T. D. Foust: Science **315** (2007) 804.

71) J. Jalak and P. Väljamäe: Biotechnol. Bioeng. **106** (2010) 871.

72) B. Yang, D. M. Willies, and C. E. Wyman: Biotechnol. Bioeng. **94** (2006) 1122.

73) T. T. Teeri: Trends Biotechnol. **15** (1997) 160.

74) T. T. Teeri, A. Koivula, M. Linder, G. Wohlfahrt, C. Divne, and T. A. Jones: Biochem. Soc. Trans. **26** (1998) 173.

75) C. Divne, J. Ståhlberg, T. Reinikainen, L. Ruohonen, G. Pettersson, J. K. Knowles, T. T. Teeri, and T. A. Jones: *Science* **265** (1994) 524.

76) J. Rouvinen, T. Bergfors, T. Teeri, J. K. Knowles, and T. A. Jones: Science **249** (1990) 380.

77) K. Kipper, P. Väljamäe, and G. Johansson: Biochem. J. **385** (2005) 527.

78) K. Igarashi, M. Wada, and M. Samejima: FEBS J. **274** (2007) 1785.

79) L. E. R. Berghem, L. G. Pettersson, and U. B. Axiofredriksson: Eur. J. Biochem. **53** (1975) 55.

80) J. R. Sellers, L. S. Weisman: in Myosins: A superfamily of molecular motors (proteins and cell regulation) (Ed., L. Coluccio), Springer (2008) 289.

81) A. D. Mehta, R. S. Rock, M. Rief, J. A. Spudich, M. S. Mooseker, and R. E. Cheney: Nature **400** (1999) 590.

82) T. Sakamoto, I. Amitani, E. Yokota, and T. Ando: Biochem. Biophys. Res. Commun. **272** (2000) 586.

83) A. Yildiz, J. N. Forkey, S. A. McKinney, T. Ha, Y. E. Goldman, and P. R. Selvin: Science **300** (2003) 2061.

84) J. N. Forkey, M. E. Quinlan, M. A. Shaw, J. E. T. Corrier, and Y. E. Goldman: Nature **422** (2003) 399.

85) D. M. Warshaw, G. G. Kennedy, S. S. Work, E. B. Krementsova, S. Beck, and K. M. Trybus: Biophys. J. **88** (2005) L30.

86) T. Sakamoto, M. R. Webb, E. Forgacs, H. D. White, and J. R. Sellers: Nature **455** (2008) 128.

87) W. Hua, J. Chung, and J. Gelles: Science **295** (2002) 844.

88) T. Okada, H. Tanaka, A. Hikikoshi Iwane, K. Kitamura, M. Ikebe, and T. Yanagida: *Biochem. Biophys. Res. Commun*. **354** (2007) 379.

89) H. E. Huxley: Science **164** (1969) 1356.

90) F. Wang, L. Chen, O. Arcucci, E. V. Harvey, B. Bowers, Y. Xu, J. A. Hammer III, and J. R. Sellers: J. Biol. Chem. **275** (2000) 4329.

91) M. A. Geeves and K. C. Holmes: Annu. Rev. Biochem. **68** (1999) 687.

92) Y. E. Goldman: Annu. Rev. Physiol. **49** (1987) 637.

93) E. M. De La Cruz, A. L. Wells, S. S. Rosenfeld, E. M. Ostap, and H. L. Sweeney: Proc. Natl. Acad. Sci. USA **96** (1999) 13726.

94) S. S. Rosenfeld and H. L. Sweeney: J. Biol. Chem. **279** (2004) 40100.

95) C. Veigel,S. Schmitz, F. Wang, and J. R. Sellers: Nature Cell Biol. **7** (2005) 861.

96) Y. Oguchi, S. V. Mikhailenko, T. Ohki, A. O. Olivares, E. M. De La Cruz, and S. Ishiwata: Proc. Natl. Acad. Sci. USA **105** (2008) 7714.

97) T. J. Purcell, H. L. Sweeney, and J. A. Spudich: Proc. Natl Acad. Sci. USA **102** (2005) 13873.

98) E. Forgacs, S. Cartwright, T. Sakamoto, J. R. Sellers, J. E. T. Corrie, M. R. Webb, and H. D. White: J. Biol. Chem. **283** (2008) 766.

99) H. Oberleithner, H. Schillers, M. Wilhelmi, D. Butzke, and T. Danker: Pflüger Arch-Eur. J. Physiol. **439** (2000) 251.

100) H. Oberleithner: J. Membrane Biol. **199** (2004) 127.

101) V. Dupres, D. Alsteens, K. Pauwels, Y. F. Dufrêne: Langmuir **25** (2009) 9653.

102) G. Andre, S. Kulakauskas, M.-P. Chapot-Chartier, B. Navet, M. Deghorain, E. Bernard, P. Hols, and Y. F. Dufrêne: Nat. Commun. **1** (2010) 27.

103) M. Maletic-Savatic, R. Malinow, and K. Svoboda: Science **283** (1999) 1923.

104) M. Matsuzaki, N. Honkura, G. C. Ellis-Davies, and H. Kasai: Nature **429** (2004) 761.

105) M. J. Kennedy, I. G. Davison, C. G. Robinson, and M. D. Ehlers: Cell **141** (2010) 524.

106) H. Makino and R. Malinow: Neuron **64** (2009) 381.

107) M. Patterson, E. M. Szatmari, and R. Yasuda: Proc. Natl. Acad. Sci. USA **107** (2010) 15951.

108) P. K. Hansma, B. Drake, O. Marti, S. A. Gould, and C. B. Prater: Science **243** (1989) 641.

109) L. Ying, A. Bruckbauer, D. Zhou, J. Gorelik, A. Shevchuk, M. Lab, Y. Korchev, and D. Klenerman: Phys. Chem. Chem. Phys. **7** (2005) 2859.

110) A. I. Shevchuk, G. I. Frolenkov, D. Sanchez, P. S. James, N. Freedman, M. J. Lab, R. Jones, D. Klenerman, and Y. E. Korchev: Angew. Chem. Int. Ed. **45** (2006) 2212.

111) D. Pastré, H. Iwamoto, J. Liu, G. Szabo, and Z. Shao: Ultramicroscopy **90** (2001) 13.

112) P. Novak, C. Li, A. I. Shevchuk, R. Stepanyan, M. Caldwell, S. Hughes, T. G. Smart, J. Gorelik, V. P. Ostanin, M. J. Lab, G. W. J. Moss, G. I. Frolenkov, D. Klenerman, and Y. E. Korchev: Nat. Methods **6** (2009) 279.

113) U. Kemiktarak, T. Ndukum, K. C. Schwa, and K. L. Ekinci: Nature **450** (2007) 85.

Legends for Figures

Fig.1 Schematic for general configuration of tapping-mode AFM system.

Fig. 2 Schematic for feedback loop and devices contained in the loop. The input to this feedback loop is the sample height variations right under the cantilever tip, and the output is z-scanner movement in the z-direction. The output from the PID controller is used as an image signal. The main time delays are indicated with τ_c for response of the cantilever oscillation amplitude to tip-sample contact, τ_p for tip parachuting, τ_m for detection of the cantilever oscillation amplitude, and τ_z for z-scanner movement.

Fig. 3 Scanner movement tracing sample surface with sinusoidal shape with periodicity of λ, without parachuting. Red broken line, trajectory of scanner movement; blue broken line, inverted trajectory of scanner movement. Difference between the blue broken line and the sample surface is tracing error.

Fig. 4 Scanning electron micrographs of small cantilevers. (A) Lever and bird-beak tip. (B) EBD tip grown on an original bird-beak tip. (C) Distal end of EBD tip before plasma etching. (D) Distal end of EBD tip after plasma etching. (E) Wing portion of previous version of small cantilever. (F) Wing portion of most recent version of small cantilever.

Fig. 5 Circuit diagrams for two types of fast amplitude detectors; (A) peak-hold type, (B) Fourier type.

Fig. 6 High-speed scanner. A sample stage (glass rod) is glued on the top surface of the z-piezoactuator using nail enamel. The z-piezoactuator is held at the four rims parallel to the displacement direction. The dimensions ($W \times L \times H$) of the z-piezoactuator are 3 $\times$ 3 $\times$ 2 mm^2. The gaps in the scanner block are filled with an elastomer for passive

damping.

Fig. 7 Active damping of z-scanner vibrations. The *LRC* circuit (mock z-scanner) is constructed so that its transfer function is similar to that of the real z-scanner.

Fig. 8 Response of cantilever oscillation amplitude while approaching to substrate surface in water and upon contacting with the surface. The gray line indicates the response of a small cantilever having an EBD tip of 1 μm long grown on the original bird-beak tip, while the black line indicates that of a cantilever with only a bird-beak tip.

Fig. 9 Structural change in bR induced by light absorption. (A) Successive high-speed AFM images of the cytoplasmic surface of D96N bR under dark or illuminated conditions. Frame rate, 1 fps; pixel size, 200 × 200 pixels. A bR trimer is highlighted by the white triangle. The green bars at 2 s and 3 s indicate illumination of 532-nm green light of 0.5 μW. (b) Schematic of arrangement of bR molecules and bR trimers under dark. The arrows indicate the directions in which respective bR molecules displace upon light illumination. (c) Schematic of arrangement of bR molecules and bR trimers under illumination. The three bR molecules in a trefoil form a transient assembly. The arrows indicate the directions in which respective bR molecules displaced upon light illumination.

Fig. 10 Dynamics of cellulose *Tr*Cel7A hydrolyzing cellulose fibers captured by HS-AFM. (A) Schematic of cellulases with two-domain structure. (B) Successive AFM images showing processive and unidirectional movement of *Tr*Cel7A on crystalline cellulose I_α. Frame rate, 1.1 fps. Three molecules are marked with the arrows with different colors. (C) Intermittent “go and stop” movement of *Tr*Cel7A molecules on cellulose I_α. The movement of seven molecules are shown with the different marks. The

broken line represents the average velocity of *Tr*Cel7A (3.5 nm/s) estimated by previous HS-AFM observation[30]. (D) Successive AFM images showing traffic jam of *Tr*Cel7A bound to crystalline cellulose III. Frame rate, 3.3 fps. The congestion is marked with the arrows. (E) Successive AFM images showing fiber peeling (marked with the arrows) of crystalline cellulose III by *Tr*Cel7A after congestion. Frame rate, 3.3 fps.

Fig. 11 Synergy between *Tr*Cel6A and *Tr*Cel7A in cellolose hydrolysis. (A) Biochemically detected synergy in cellobiose production from cellulose IIII. The plots with green and red closed circles are the rates of cellobiose production by *Tr*Cel6A and *Tr*Cel7A, respectively, and the plot with blue closed circles shows the synergy between the two enzymes. The dotted black line indicates the simple sum of cellobiose production calculated from the plots with green and red closed circles. (B) Successive AFM images showing crystalline cellulose III fibers being hydrolyzed by *Tr*Cel6A alone. No appreciable degradation of the fibers is observed. The time shown in each image indicates a lapse after the addition of *Tr*Cel6A. Frame rate, 3.3 fps. (C) Successive AFM images showing rapid degradation of crystalline cellulose III fibers in the presence of both *Tr*Cel6A and *Tr*Cel7A. *Tr*Cel7A was added at 8.3 min after the initial addition of *Tr*Cel6A. The time shown in each image indicates a lapse after the addition of *Tr*Cel7A. Frame rate, 3.3 fps.

Fig. 12 Walking M5-HMM captured by HS-AFM. (A) Successive AFM images showing processive movement of M5-HMM in 1 μM ATP. Frame rate, 7 fps. (B) Schematic of two-headed bound M5-HMM. (C) Successive AFM images showing hand-over-hand movement in 1 μM ATP. Frame rate, 7 fps. The swinging lever is highlighted with a thin white line. (D) Schematic explaining the images in C. The marks

“+” indicates the plus ends of actin filaments.

Fig. 13 Other dynamic events of M5 HMM observed by HS-AFM. (A) Unfolding of coiled-coil tail of two-headed bound M5-HMM. Top image, before unfolding; bottom image, after unfolding. (B) Successive AFM images showing foot stomp at leading head observed in 1 μM ATP. The events of leading head detachment from actin are indicated with the arrow heads. Imaging rate, 7 fps. (C) AFM image showing sharply bent leading head of two-headed bound M5-HMM in the nucleotide-free condition. The makrs “+” indicate the plus ends of actin filaments.

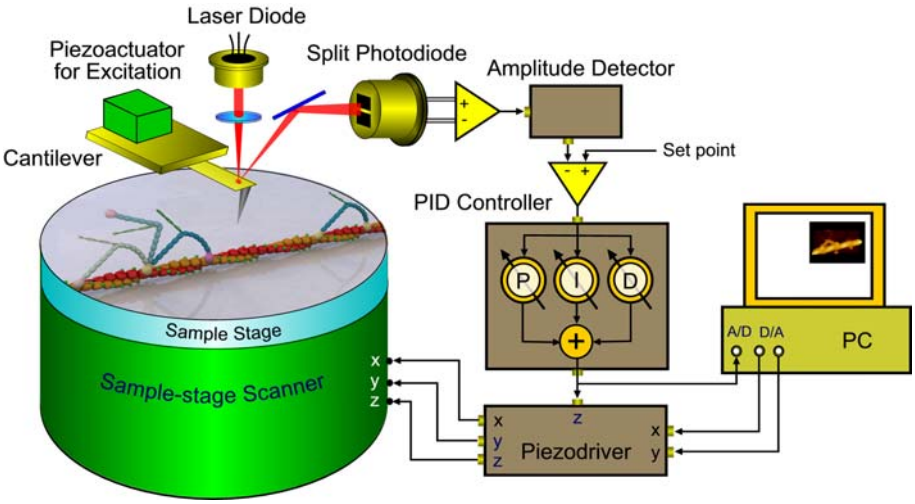
Laser Diode
Piezoactuator for Excitation
Split Photodiode
Amplitude Detector
Cantilever
Set point
PID Controller
P
I
D
Sample Stage
Sample-stage Scanner
x
y
z
A/D D/A
PC
Piezodriver

Figure 1

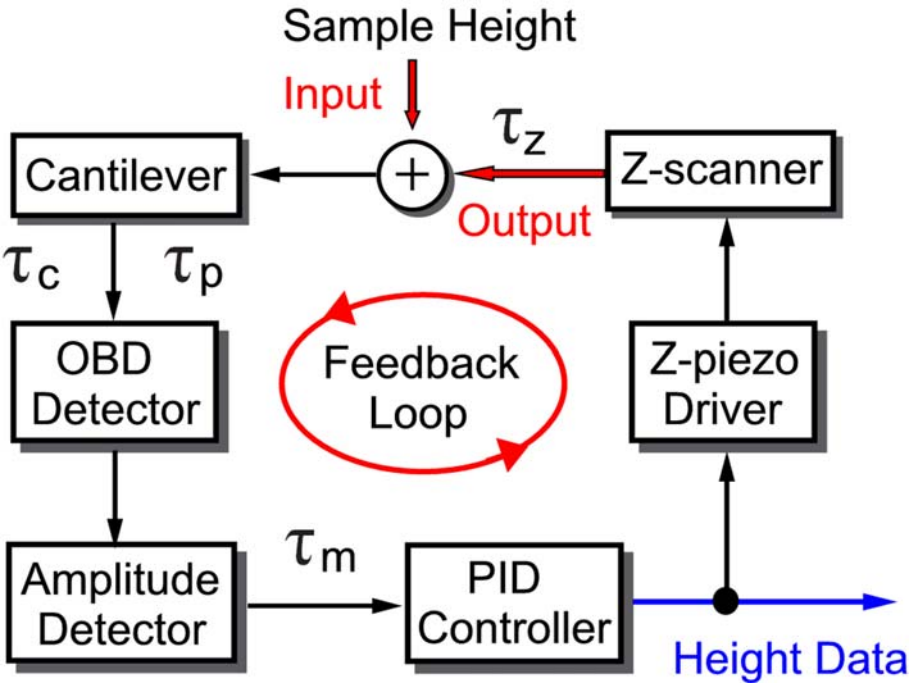
Sample Height
Input
τ_z
Cantilever
Z-scanner
Output
τ_c
τ_p
OBD
Detector
Feedback
Loop
Z-piezo
Driver
Amplitude
Detector
τ_m
PID
Controller
Height Data

Figure 2

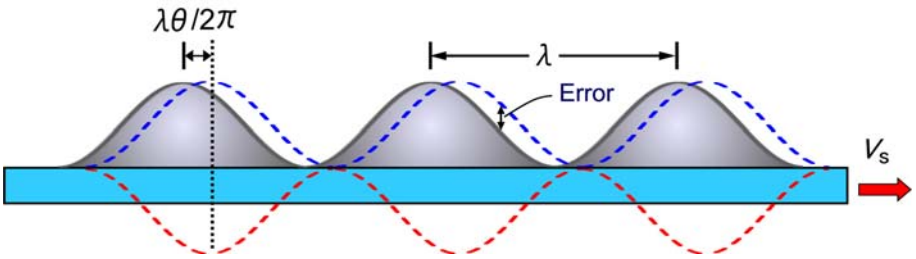

Figure 3

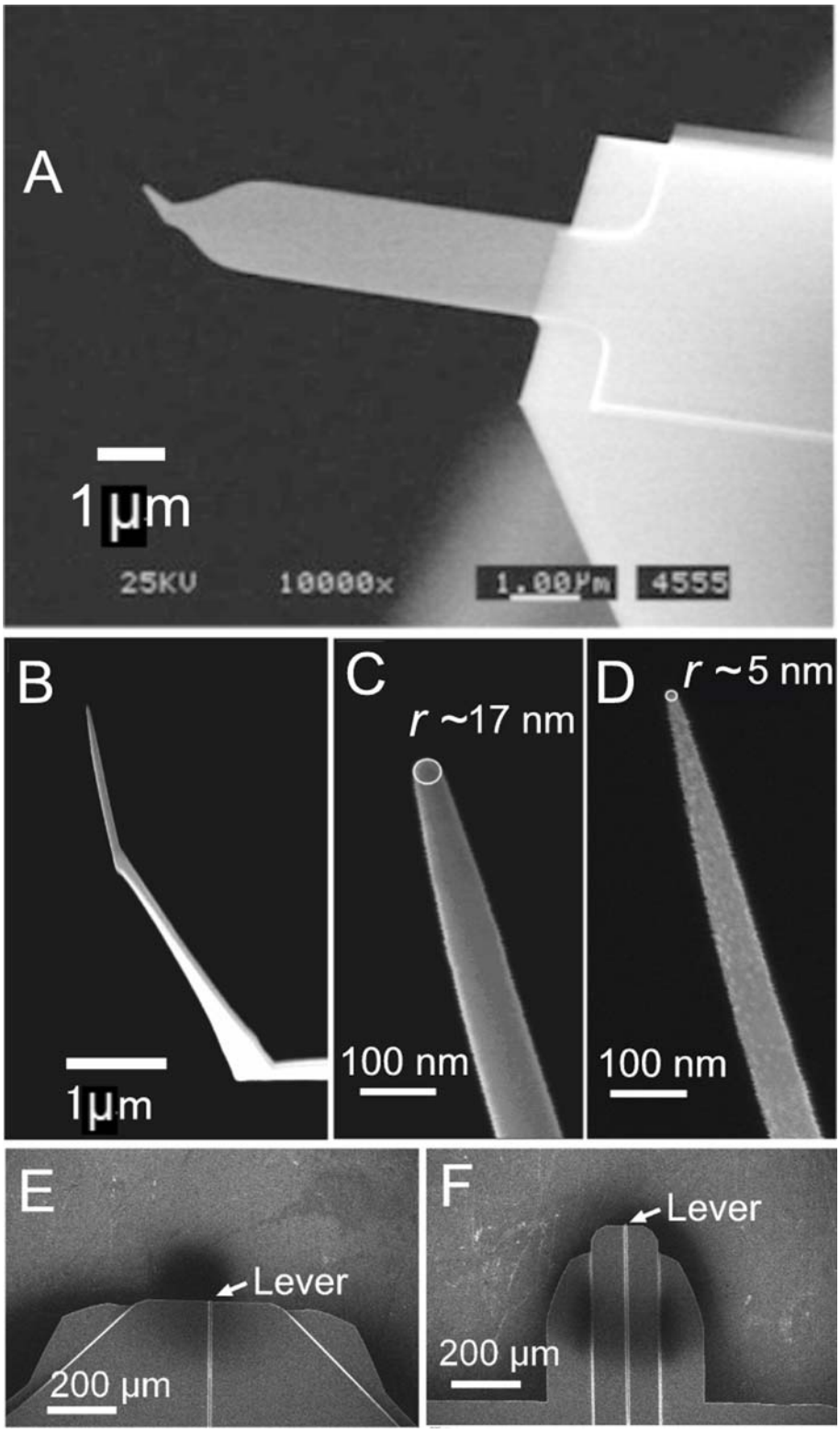
A
1 µm
25KV
10000x
1.00µm
4555
B
1µm
C
r ~17 nm
100 nm
D
r ~5 nm
100 nm
E
Lever
200 µm
F
Lever
200 µm

Figure 4

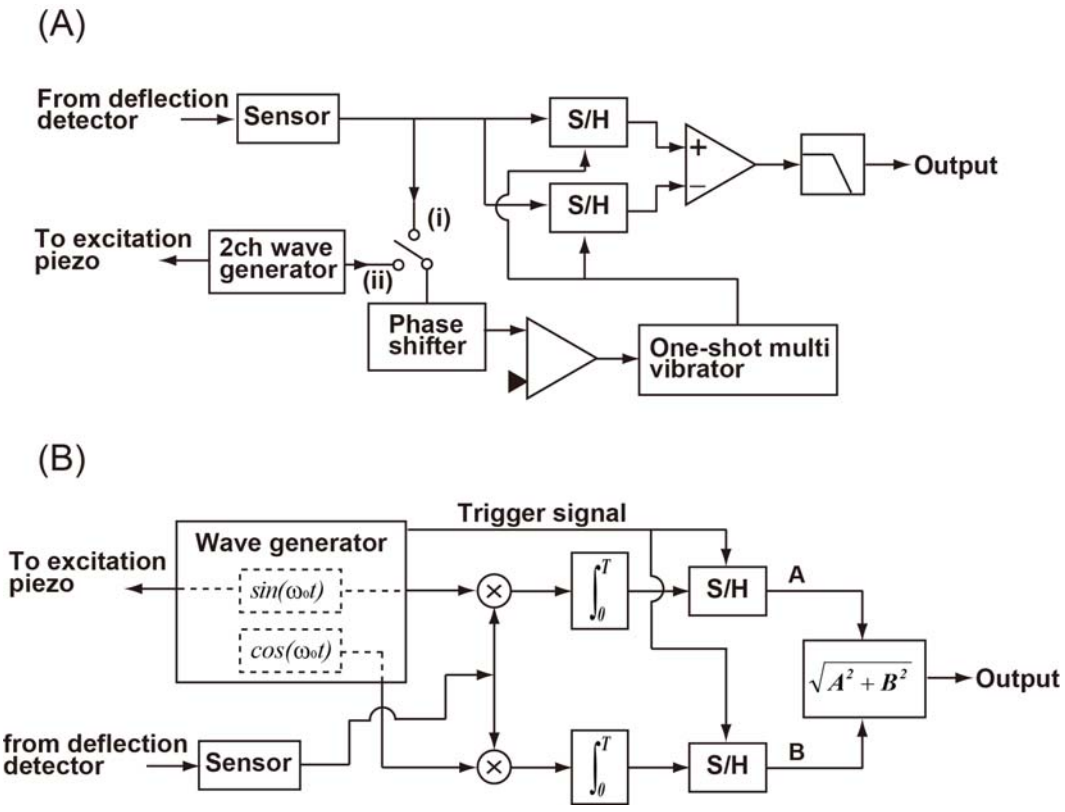
(A)
From deflection detector
Sensor
S/H
S/H
+
−
Output
(i)
To excitation piezo
2ch wave generator
(ii)
Phase shifter
One-shot multi vibrator
(B)
Trigger signal
Wave generator
To excitation piezo
sin(ω₀t)
cos(ω₀t)
S/H
A
√(A² + B²)
Output
from deflection detector
Sensor
S/H
B

Fig. 5

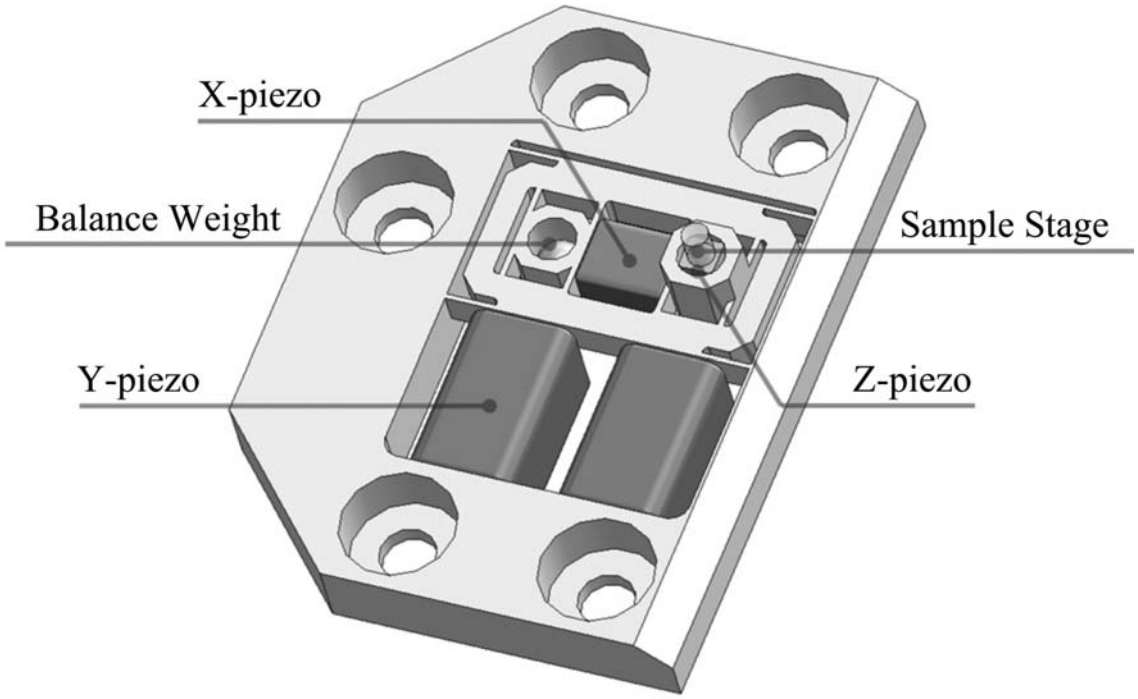

Figure 6

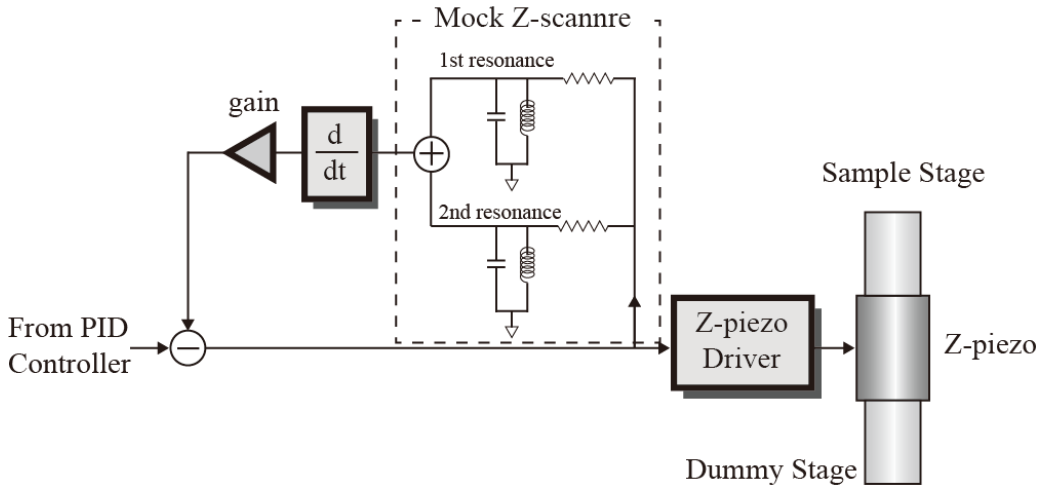
Mock Z-scannre
1st resonance
gain
d
dt
2nd resonance
Sample Stage
From PID
Controller
Z-piezo
Driver
Z-piezo
Dummy Stage

Fig. 7

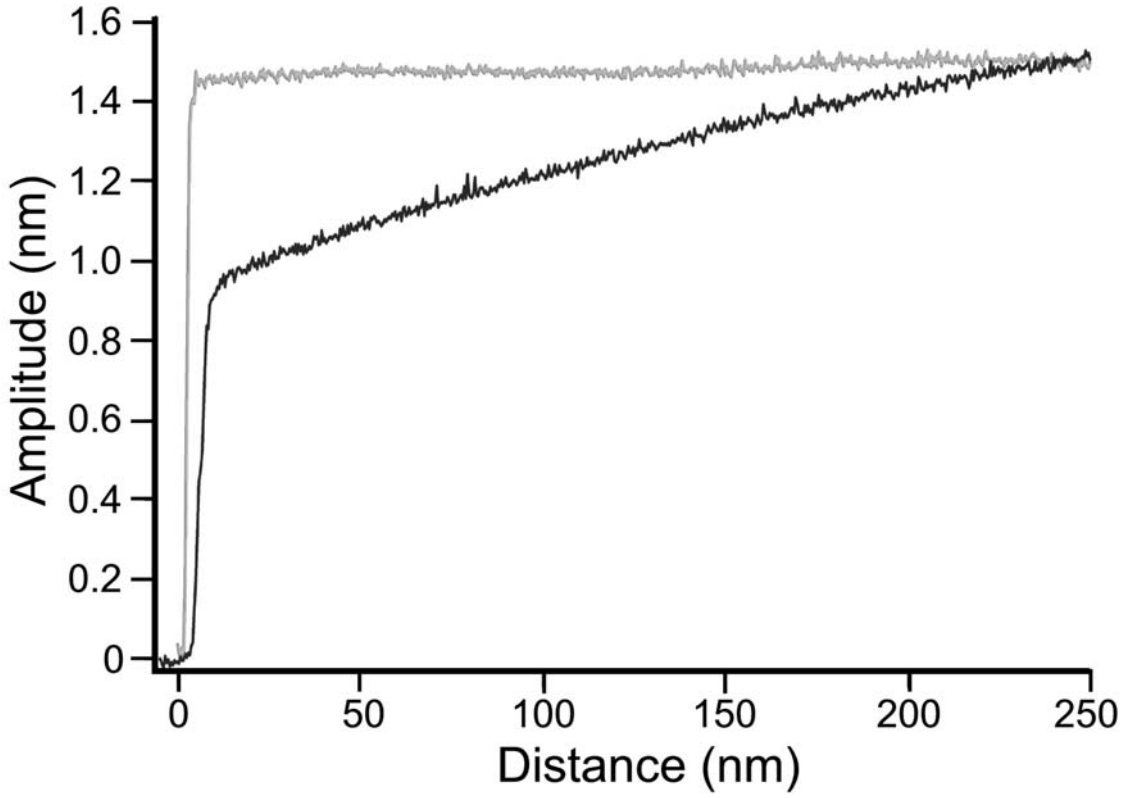
Amplitude (nm)
1.6
1.4
1.2
1.0
0.8
0.6
0.4
0.2
0
0
50
100
150
200
250
Distance (nm)

Figure 8

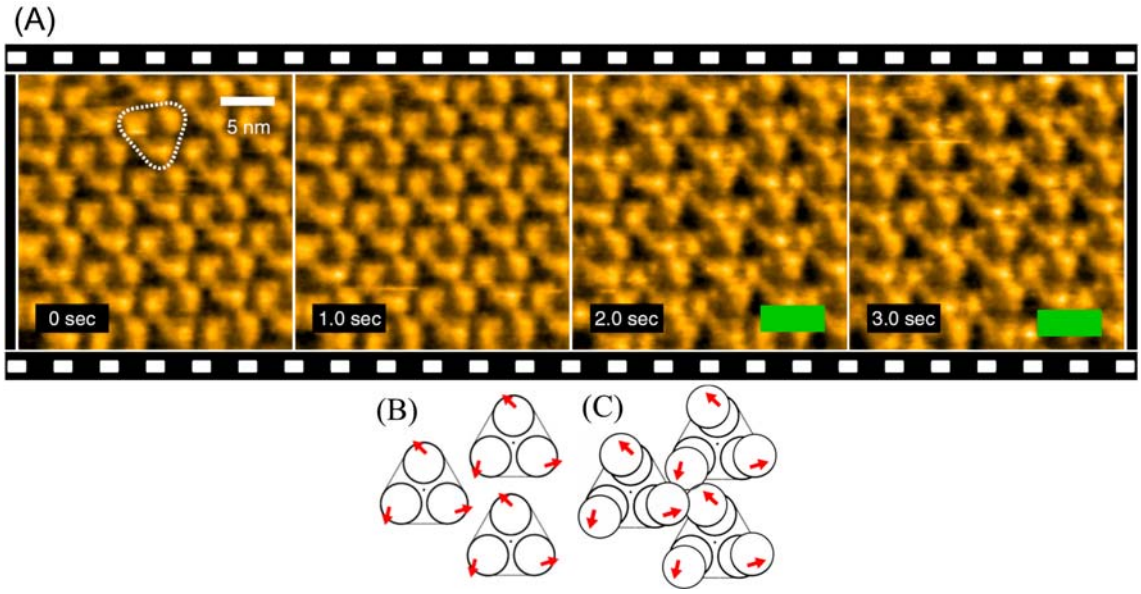

Figure 9

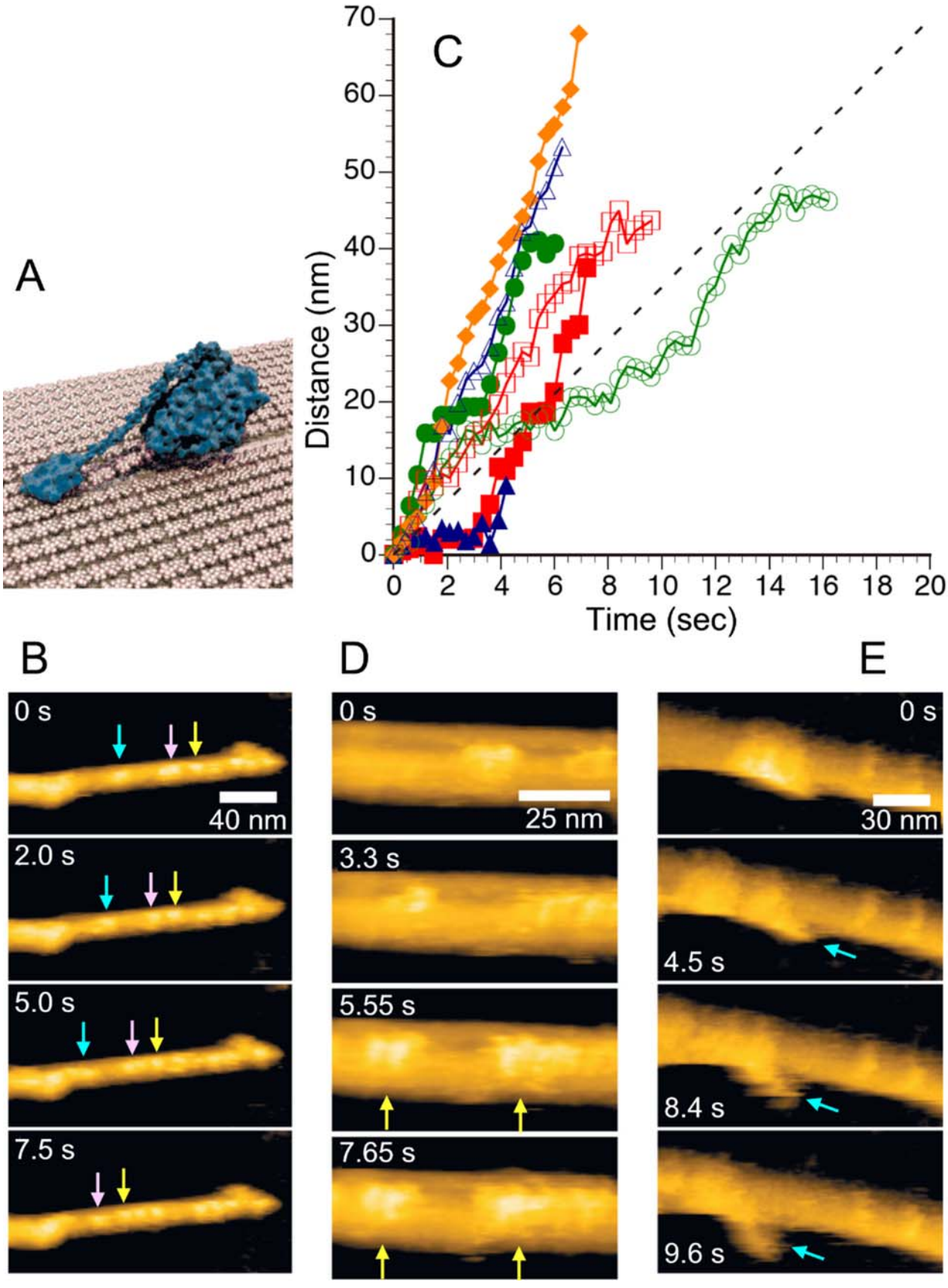
A
C
Distance (nm)
Time (sec)
B
D
E
0 s
40 nm
2.0 s
5.0 s
7.5 s
25 nm
3.3 s
5.55 s
7.65 s
30 nm
4.5 s
8.4 s
9.6 s

Figure 10

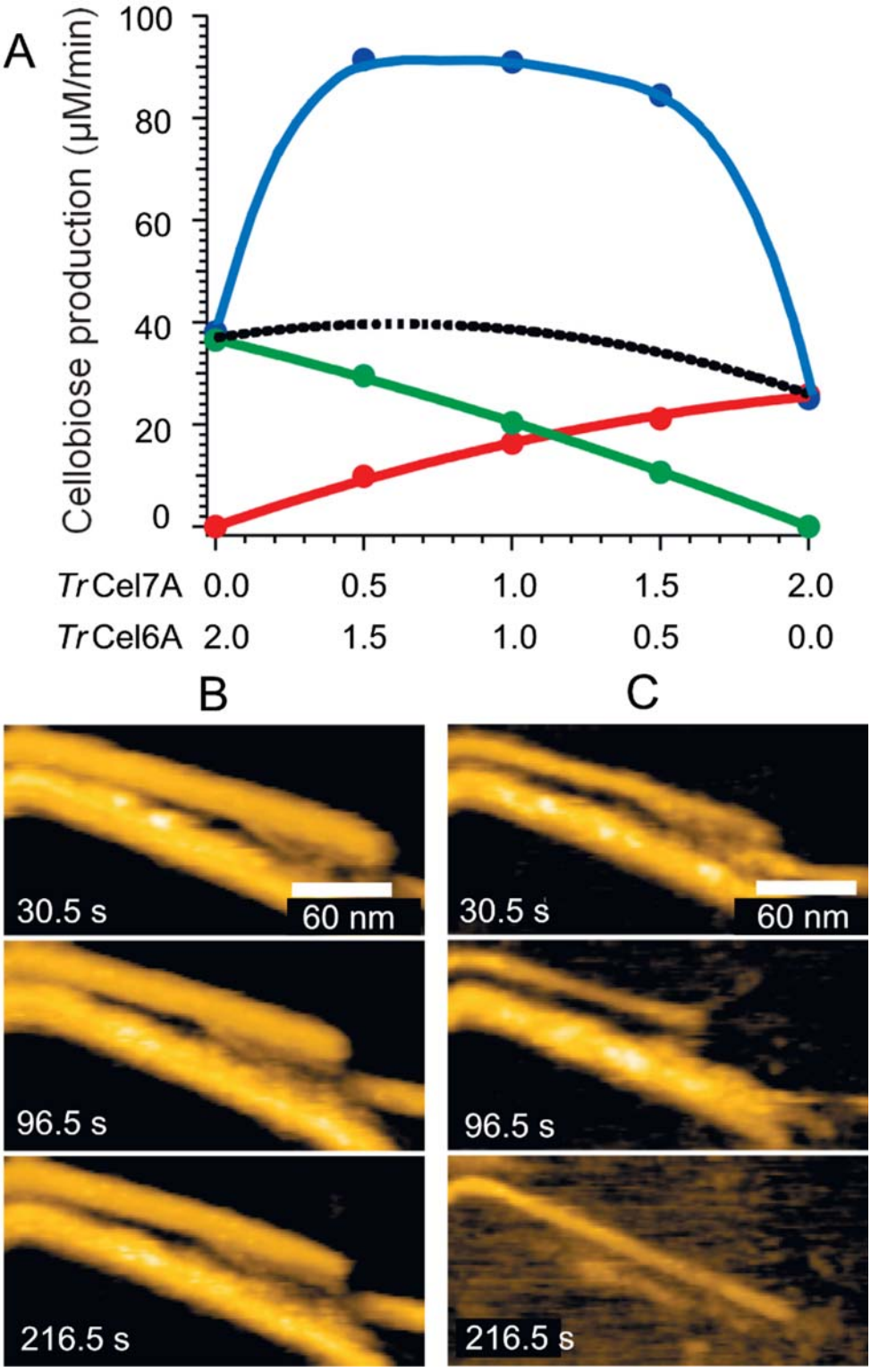
A
Cellobiose production (μM/min)
100
80
60
40
20
0
TrCel7A 0.0 0.5 1.0 1.5 2.0
TrCel6A 2.0 1.5 1.0 0.5 0.0
B
C
30.5 s
60 nm
96.5 s
216.5 s
30.5 s
60 nm
96.5 s
216.5 s

Figure 11

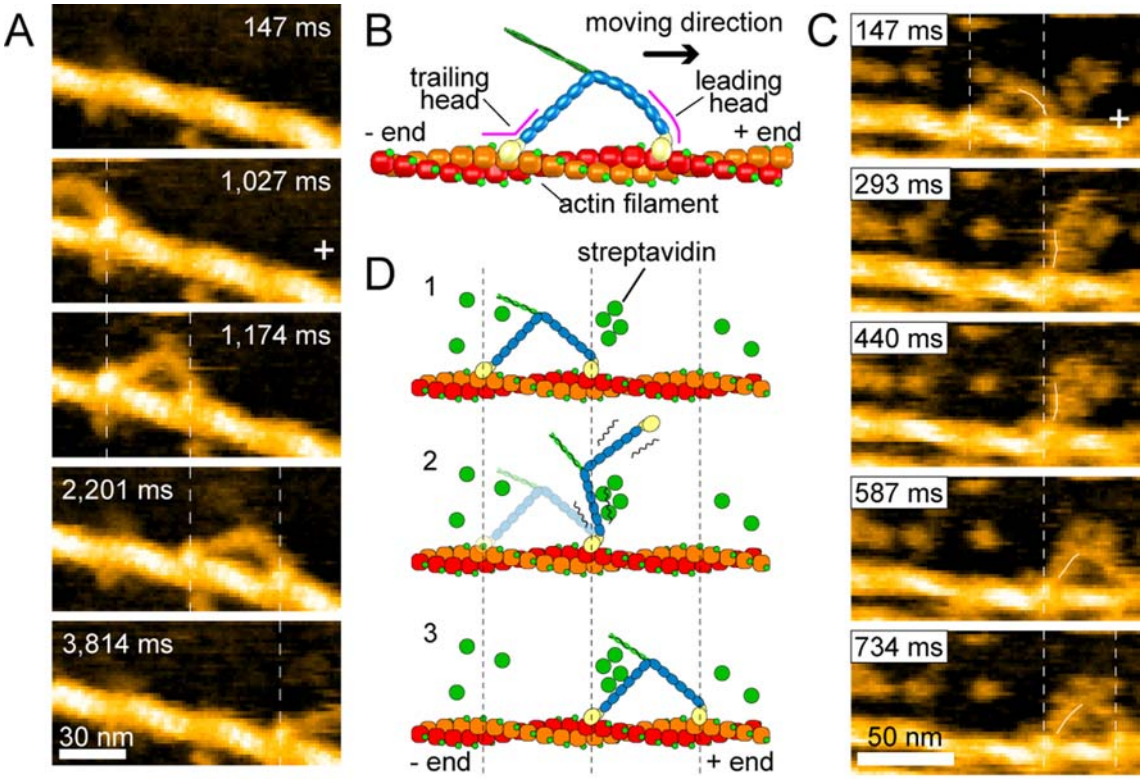
A
147 ms
1,027 ms
+
1,174 ms
2,201 ms
3,814 ms
30 nm
B
moving direction
trailing head
leading head
- end
+ end
actin filament
D
streptavidin
1
2
3
- end
+ end
C
147 ms
+
293 ms
440 ms
587 ms
734 ms
50 nm

Figure 12

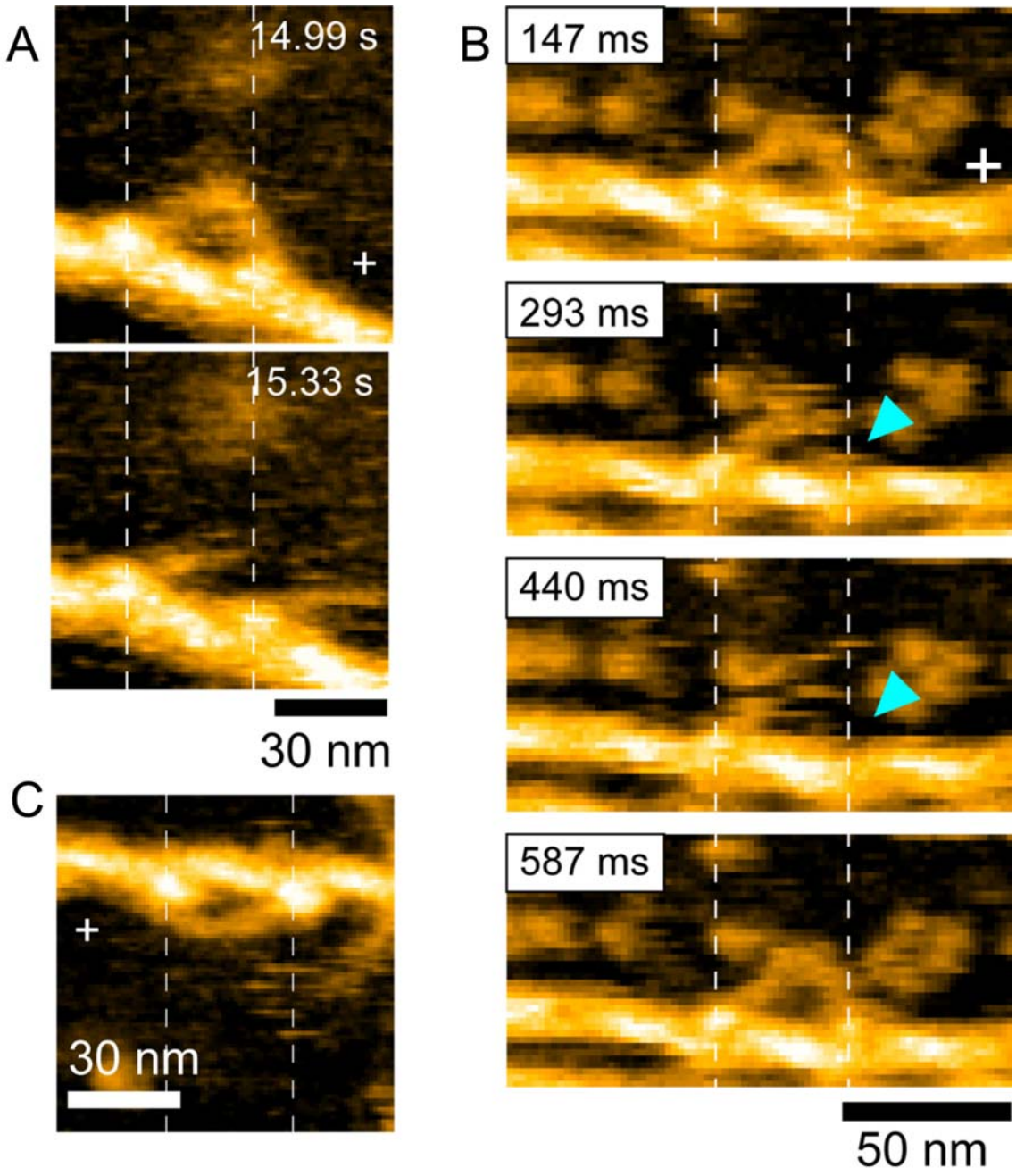

Figure 13